附件一

行政院國家科學委員會補助專題研究計畫 ☑ 成 果 報 告 □期中進度報告

介觀結構的失相、暫態反應、量子傳輸等特性的研究(3/3)

A study on the dephasing, transient responses, and quantum transport in mesoscopic structures (3/3)

計畫類別：☑ 個別型計畫　　□ 整合型計畫
計畫編號：NSC 92 － 2112 － M － 009 － 035 －
執行期間： 2003 年 08 月 01 日至 2004 年 07 月 31 日

計畫主持人：朱仲夏 教授
共同主持人：
計畫參與人員：唐志雄,鄔其君, 鐘淑維,王律堯,林昱佑,林哲民,簡靖航,
陳淑娟,黃宇廷,吳昭偉

成果報告類型(依經費核定清單規定繳交)：□精簡報告 ☑完整報告

本成果報告包括以下應繳交之附件：
□赴國外出差或研習心得報告一份
□赴大陸地區出差或研習心得報告一份
☑出席國際學術會議心得報告及發表之論文各一份
□國際合作研究計畫國外研究報告書一份

處理方式：除產學合作研究計畫、提升產業技術及人才培育研究計畫、列管計畫及下列情形者外，得立即公開查詢
□涉及專利或其他智慧財產權，□一年□二年後可公開查詢

執行單位：國立交通大學電子物理系

中 華 民 國 93 年 12 月 15 日

行政院國家科學委員會專題研究計劃成果報告

介觀結構的量子傳輸: (一)開放式量子點在時變場下的傳輸；(二)利用 ac 閘極來產生和量測自旋流；(三)指狀閘極陣列結構的量子幫浦的特性與機制；(四)在 Rashba-type 的量子通道中產生 dc 自旋流；(五)振盪位能對於介觀環與電子熱庫耦合的效應；(六)兩接頭的介觀環的 Fano 共振傳輸的研究。

The quantum transport in mesoscopic structure: [I] Transport spectroscopic in a time-modulated open quantum-dot; [II] Spin current generation and detection in the presence of an ac gate; [III] Finger-gate array quantum pumps: pumping characteristics and mechanisms; [IV] Dc spin current generation in a Rashba-type quantum channel; [V]Effect of an oscillating potential on the persistent current transition in a mesoscopic ring coupled to an electron reservoir; [VI] Fano resonance transport through a mesoscopic two-lead ring.

一、中文摘要:

在本計劃中，我們研究了介觀系統中的量子傳輸，其中包括(一)開放式量子點在時變場下的傳輸；(二)利用 ac 閘極來產生和量測自旋流；(三)指狀閘極陣列結構的量子幫浦的特性與機制；(四)在 Rashba-type 的量子通道中產生 dc 自旋流；(五)介觀環結構的失相；(六)兩接頭的介觀環的 Fano 共振傳輸的研究。

(一)開放式量子點在時變場下的傳輸：我們研究在有時變調制的開放式量子點中，我們使用時間相關模的匹配方法去計算電導 G 以及電子的 dwell time；在高頻的情況下，傳導電子展現出三種不同的共振散射行為；藉由 intersideband 散射躍遷至：量子點中的準束縛態；量子點中的真束縛態；以及接頭中 subband threshold 下面的準束縛態。電導 G 中顯示出 Dip 和 Fano 結構等特徵。我們的結果也觀察到 inter- sideband $2\hbar\omega$的躍遷過程。

(二)利用 ac 閘極來產生和量測自旋流：我們研究在 III-V 族窄能隙的量子阱或量子線中，可以利用一個時變的閘極去影響 Rashba 自旋軌道耦合係數來產生自旋流。我們也提出對此交流自旋流的整流方法，以及利用電性量測去測量在二維電子氣中帶有交流自旋流的閘極附近的電壓以達到偵測自旋流之目的；我們提出一種不需要使用光學或磁性材料來達到"產生"和"偵測"自旋流的方法。

(三)指狀閘極陣列結構的量子幫浦的特性與機制：我們研究在量子窄通道中一對指狀閘極有限的陣列結構中，緩變以及非緩變情況下的幫浦效應；幫浦位能是由外加的交流偏壓的指狀閘極陣列提供，我們藉此建構出幫浦的物理性質以及機制，在單一對(N=1)指狀閘極結構中，幫浦機制是由於同調非彈性散射使傳導電子躍遷至 subband threshold 所引起的；對於兩對以上(N>2)的結構，主要幫浦機制是由時間相關的布拉格反射(Bragg reflection)所造成。布拉格反射對於幫浦的貢獻是由於幫浦位能佔優勢的傳遞形式使電子的穿透率對稱性被破壞所引起；我們可以藉由調整指狀閘極陣列結構配置和每對外加交流偏壓的指狀閘極間的相位差ϕ來達成傳遞波的條件。我們也利用 N=4 的指狀閘極陣列結構來研究量子幫浦的機制。

(四)在 Rashba-type 的量子通道中產生 dc 自旋流：我們提出了共振非彈性散射(RIS)對於直流(dc)自旋流扮演了一個重要的角色，這個共振非彈性散射可以使一個簡單的閘極結構產生直流自旋流；我們利用單一個外加交流偏壓指狀閘極，放在有 Rashba 自旋軌道交互作用的量子窄通道上；這個有交流偏壓的指狀閘極會使 Rashba 耦合係數產生時間調制，造成與自旋有關的共振非彈性散射，而產生直流自旋流。自旋流產生要同時存穩態與動態的自旋軌道耦合係數 α_0 以及 α_1，而產生的自旋流大小正比於 $\alpha_0\alpha_1^2$。我們提出這樣一個構想的優點是不會有直流電荷流產生；我們的結果也顯示出可以利用雙指狀閘極結構來有效增加自旋流。

(五)振盪位能對於介觀環與電子熱庫耦合的效應：我們研究震盪位能對於在一個介觀環與電子熱庫耦合的持續電流(persistent current)的效應；環除了有外加的磁通量外也具有部分的同調性，使得電子可以藉由震盪位能來產生非彈性散射；我們採取 Büttiker 的模型來處理非同調散射問題，這個方法使我們能夠研究震盪位能對於一個固定電子數目的環中所產生持續電流的影響。我們使用巨正則系綜來處理電子的數目；我們結果顯示出當位能震盪頻率接近或快過於傳播的電子時，持續電流顯示出多 peak 的結構，電子除了在最高能階會產生持續電流的躍遷，在最高能階以下也會滿足共振條件。相對的，當電子只有最高能階的共振躍遷發生時，指會顯示出持續電流的 peak 結構。

(六)兩接頭的介觀環的 Fano 共振傳輸的研究：我們研究在無外加磁場情況下有兩個接頭的一維介觀環的傳輸現象；我們發現 Fano 共振現象在沒有良好定義的準束縛態一樣會發生。結果顯示在開放式的環中，當能量符合介觀環的駐波條件時會產生 Fano 結構；但是在一些特殊的能量條件下這些 Fano 結構的寬度會慢慢變窄甚至消失。我們發現 Fano 結構不一定是傳統上認為共振與非共振的連續態所造成的結果，我們可以利用奈米製程以及電性量測來控制系統參數用以調制 Fano 結構。

Abstract:

We study the quantum transport in mesoscopic structure: [I] Transport spectroscopic in a time-modulated open quantum-dot; [II] Spin current generation and detection in the presence of an ac gate; [III] Finger-gate array quantum pumps: pumping characteristics and mechanisms; [IV] Dc spin current generation in a Rashba-type quantum channel; [V] Effect of an oscillating potential on the persistent current transition in a mesoscopic ring coupled to an electron reservoir; [VI] Fano resonance transport through a mesoscopic two-lead ring.

[I] Transport spectroscopic in a time-modulated open quantum-dot:
We have investigated the time-modulated coherent quantum transport phenomenon in a ballistic open quantum dot. Conductance G and the electron dwell time in the dots are calculated by a time-dependent modematching method. Under high-frequency modulation, the traveling electrons are found to exhibit three types of resonant scatterings. They are intersideband scatterings into quasibound states in the dots, into true bound states in the dots, and into quasibound states in the just beneath the subband threshold in the leads. Dip structures or fano structures in G are their signatures. Our results show structures due to $2\hbar\omega$ intersideband processes. At the above scttering resonances, we have estimated, according to our dwell time calculation, the number of round-trip scatterings which the traversing electrons undertake between two dot openings.

[II] Spin current generation and detection in the presence of an ac gate：
We predict that in a narrow gap III-V semiconductor quantum well or quantum wire, an observable electron spin current can be generated with a time-dependent gate to modify the Rashba spin-orbit coupling constant. Methods to rectify the so generated ac current are discussed. An all-electric method spin-current detection is suggested, which measures the voltage on the gate in the vicinity of a two-dimensional electron gas carrying a time-dependent spin current. Both the generation and detection do not involve any optical or magnetic mediator.

[III] Finger-gate array quantum pumps: pumping characteristics and mechanisms：
We study the pumping effects, in both the adiabatic and nonadiabatic regimes, of a pair of finite finger-gate array (FGA) on a narrow channel. Connection between the pumping characteristics and associated mechanisms is established. The pumping potential is generated by ac biasing the FGA pair. For a single pair (N=1) of finger gates (FG's), the pumping mechanism is due to the coherent inelastic scattering of the traversing electron to its subband threshold. For a pair of FGA with pair number N>2, the dominant pumping mechanism becomes that of the time-dependent Bragg reflection. The contribution of time-dependent Bragg reflection to the pumping is enabled by breaking the symmetry in the electron transmission when the pumping potential is of a predominant propagating type. This propagating wave condition can be achieved both by an appropriate choice of the FGA pair configuration and by the monitoring of a phase difference ϕ between the ac biases in the FGA pair. The robustness of such a pumping mechanism is demonstrated by considering a FGA pair with only pair number N=4.

[IV] Dc spin current generation in a Rashba-type quantum channel：
We propose and demonstrate theoretically that resonant inelastic scattering (RIS) can play an important role in dc spin current generation. The RIS makes it possible to generate dc spin

current via a simple gate configuration: a single finger-gate that locates atop and orients transversely to a quantum channel in the presence of Rashba spin-orbit interaction. The ac biased finger-gate gives rise to a time-variation in the Rashba coupling parameter, which causes spin-resolved RIS, and subsequently contributes to the dc spin current. The spin current depends on both the static and dynamic parts in the Rashba coupling parameter, α_0 and α_1, respectively, and is proportional to $\alpha_0\alpha_1^2$. The proposed gate configuration has the added advantage that no dc charge current is generated. Our study also shows that the spin current can be enhanced significantly in a double finger-gates configuration.

[V] Effect of an oscillating potential on the persistent current transition in a mesoscopic ring coupled to an electron reservoir：

We have investigated the effect of an oscillating potential on the time-averaged persistent current in a mesoscopic ring coupled to an electron reservoir. The ring is not only threaded by a magnetic flux but also partially coherent such that the conduction electrons in the ring will come across inelastic scattering due to the oscillating potential. A S-matrix model which is proposed by M. Büttiker for incoherence scattering has been adopted in our situation. This model allows us to study how the oscillating potential affects the persistent current when the ring contains fixed number of electrons. A grand canonical ensemble approach is presented to settle the number of electrons. Our results demonstrate that when the oscillating frequency of the barrier is close to or faster than that of the traversing electrons, the persistent current lead to multi-peak transition. Moreover, not only will one electron on the highest level in the ring lead to the persistent current transition but the electrons below the highest level will as long as they satisfy the resonance condition. On the contrary, only one persistent current resonance peak occurs and the electrons occupied on the highest level will invoke transition. A physical interpretation is presented.

[VI] Fano resonance transport through a mesoscopic two-lead ring：

The low-energy and ballistic transport through a 1-dimensional two-lead ring at zero magnetic field is studied. We find Fano resonance even in the absence of well-defined quasibound states, and its appearance depends sensitively on the commensurability of the system parameters. Our study have focused on the case of the potential in the ring defines open but not closed cavities, and it is found that Fano resonance may appear at energies correspond to the standing wave states in the ring, but commensurate system parameters can shrink the widths of the resonance at some energies to infinitesimally small. These findings suggest that the conventional picture of the Fano resonance as an effect due to the interference between the paths through resonant states and non-resonant continuum of states might not account for all the Fano-type lines seen in the transport measurements. Moreover, the resonance may find application in the fabrication of electrical nano-devices since it is sensitive to the system parameters and hence tunable.

Keywords:

Quantum transport, quasi-bound state, time-dependent inelastic scattering, quantum channel, spin current, mesoscopic ring, Fano structures, dwell time, persistent current.

二、Motivations and goals

[I] Transport spectroscopic in a time-modulated open quantum-dot:

In the past decade, the quantum transport phenomenon in open quantum dots has received much attention.[1–11] The open quantum dot, consisting of a submicron sized cavity connecting via point contact leads to two end-electrodes, has become an important device for the investigation of phasecoherent processes and their various mechanisms. The size of the dot and the width of the leads can be controlled by split gates. In high electron mobility samples, and at sufficient low temperatures, the phase-coherent length may well exceed the dimension of the device, allowing electrons to remain coherent while traversing the dot.

[II] Spin current generation and detection in the presence of an ac gate:

One key issue in spintronics based on semiconductor is the efficient control of the spin degrees of freedom. Datta and Das [12] suggested the use of gate voltage to control the strength of Rashba spin-orbit interaction (SOI) [13] which is strong in narrow gap semiconductor heterostructures. In InAs-based quantum wells a variation of 50% of the SOI coupling constant was observed experimentally. [14,15] Consequently, much interest has been attracted to the realization of spin-polarized transistors and other devices based on using electric gate to control the spin-dependent transport [16]. In addition to using a static gate to control the SOI strength and so control the stationary spin transport, new physical phenomena can be observed in time-dependent spin transport under the influence of a fast varying gate voltage. Along this line, in this article we will consider a mechanism of ac spin current generation using time-dependent gate. This mechanism employs a simple fact that time variation of Rashba SOI creates a force which acts on opposite spin electrons in opposite directions. Inversely, when a gate is coupled to a nearby electron gas, the spin current in this electron gas also induces a variation of the gate voltage, and hence affects the electric current in the gate circuit. We will use a simple model to clarify the principle of such a new detection mechanism without any optical or magnetic mediator. The systems to be studied will be 1D electron gas in a semiconductor quantum wire (QWR) and 2D electron gas in a semiconductor quantum well (QW).

[III] Finger-gate array quantum pumps: pumping characteristics and mechanisms：

Quantum charge pumping (QCP) has become an active field in recent years.[17-37] This is concerned with the generation of net transport of charges across an unbiased mesoscopic structure by cyclic deformation of two structure parameters. Original proposal of QCP, in the adiabatic regime, was due to Thouless [17,18] and Niu. [18] They considered the current generated by a slowly varying traveling wave in an isolated one-dimensional system. The number of electrons transported per period was found to be quantized if the Fermi energy lies in a gap of the spectrum of the instantaneous Hamiltonian. Aiming at this quantized pumped charge nature of the adiabatic pumping, Niu proposed various one-dimensional periodic potentials for the adiabatic quantum pumping (AQP), [18] and pointed out the importance of the quantized charge pumping in utilizing it for a direct-currentstandard. [18]

[IV] Dc spin current generation in a Rashba-type quantum channel：

Spintronics is important in both application and fundamental arenas [38, 39]. A recent key issue of great interest is the generation of dc spin current (SC) without charge current. Various dc SC generation schemes have been proposed, involving static magnetic field [40, 41], ferromagnetic

material [42], or ac magnetic field [43]. More recently, Rashba-type spin-orbit interaction in 2DEG [44, 45] has inspired attractive proposals for nonmagnetic dc SC generation [46-48]. Of these recent proposals, including a time-modulated quantum dot with a static spin-orbit coupling [46], and time-modulations of a barrier and the spin-orbit coupling parameter in two spatially separated regions [47], the working principle is basically adiabatic quantum pumping. Hence simultaneous generation of both dc spin and charge current is the norm. The condition of zero dc charge current, however, is met only for some judicious choices for the values of the system parameters.

[V] Effect of an oscillating potential on the persistent current transition in a mesoscopic ring coupled to an electron reservoir：

Persistent current in the mesoscopic conducting ring which is threaded by a the magnetic flux has invoked a great number of interests in quantum transport. Since the implementation in experimental apparatus could be enforced. [49]Additionally, the mesoscopic systems due to a periodic in time modulation are now of considerable interest. It has been pointed out [50] hat when particles carrying energy E incident through a time-

dependent barrier, which is in the form of $V(x;\ t) = V_0(x) + V_1(x;\ t)$, it will emit or absorb modulation quanta because of interacting with the perturbation $V(x)\cos(\omega t)$. The perturbation of the form $V(x;\ t)$ has a width of d. The comparison between the traversal time of the particle interacting with the barrier and the period of the oscillating potential has two main physical features. One of the features is that if the oscillating frequency is low when compared with the traversal time of particles, then the particle will see an effective static barrier during its travel. However, it is different for the other feature when the barrier is at high frequency. In this situation, the particle will see several cycles of oscillation. This paper explores traversal time of the particles going through the oscillating barrier with width d.

[VI] Fano resonance transport through a mesoscopic two-lead ring：

The conventional Fano resonance is an effect due to the interference between resonant and non-resonant processes. It was first proposed in atomic physics [51], and the effect was then observed in a wide variety of spectroscopy such as the atomic photoionization [52], optical absorption [53], Raman scattering [54], and neutron scattering [55]. As recent progress in the technology of fabrication of electrical nano-devices has achieved devices with the size of the order of the inelastic length scales of the conduction electrons, where within the electronic transport is ballistic, the Fano resonance is also seen in condensed matter systems. For instance, it is seen in the Scanning Tunneling Spectroscopy of a surface impurity atom [56,57], transport through a quantum dot (QD) [58-63] or carbon nanotube [64]. Moreover, it is proposed that the resonance can be used in the probe of phase coherence [65,66] and design of spin filters [67].

三、Results and discussion:

We have studied: **[I] Transport spectroscopic in a time-modulated open quantum-dot [68]. (Appendix A).**

[II] Spin current generation and detection in the presence of an ac gate [69]. (Appendix B).

[III] Finger-gate array quantum pumps: pumping characteristics and mechanisms [70] (Appendix C).

[IV] Dc spin current generation in a Rashba-type quantum channel [71] (Appendix D).

[V] Effect of an oscillating potential on the persistent current transition in a mesoscopic ring coupled to an electron reservoir：

We have investigated an interesting phenomenon about the difference between the incoherence time of the electrons in the ring and the oscillating time of the barrier exhibited in a partially-coherent ring. the system configuration is shown in Fig. 1. The qualitative difference has been demonstrated. When incoherence time of the electrons in the ring is dominated, the characteristic of the number current as a function of flux present a single peak figure. This result is shown in Fig. 2. For the case that when the oscillating frequency of the barrier is close to or faster than that of the traversing electrons, however, multi peak persistent current transition appears in Fig. 3. In the former situation only the electron on the highest levels is induced. However, for the latter situation total electrons on the highest levels are excited to appropriate energy levels. This physical mechanism is studied in detail and the coherence nature of the ring is elucidated in this paper. This particular feature allows us to have a deeper understanding on the topic of quantum transport in a mesoscopic ring.

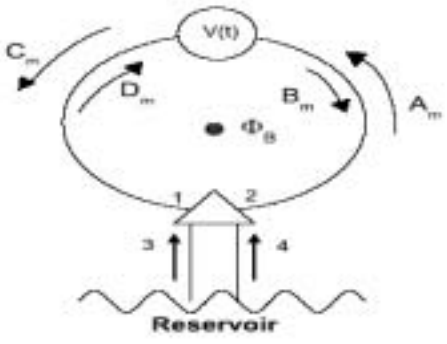

Fig. 1: This configuration illustrates a partially coherent ring coupled an electron reservoir with oscillating potential $V(t)$ and a magnetic flux Φ_B in the center of the ring.

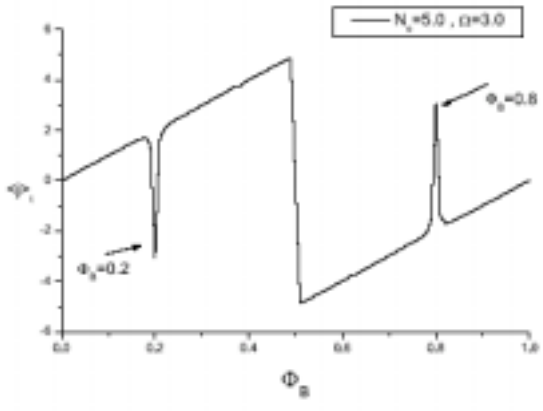

Fig. 2: $\langle j \rangle_t$ as a function of flux for fixed number of electrons $N_e = 5$ and the oscillating frequency $\Omega = 3.0$.

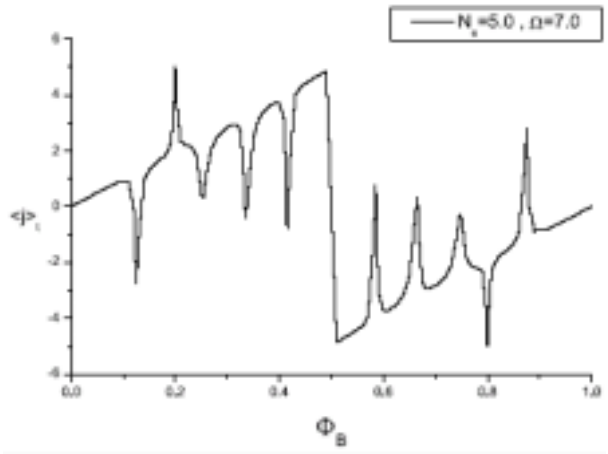

Fig. 3: $\langle j \rangle_t$ as a function of flux for fixed number of electrons $N_e = 5$ and the oscillating frequency $\Omega = 7.0$.

[VI] Fano resonance transport through a mesoscopic two-lead ring.

a. Unequal armlengths:

The system structure is shown in Fig. 4. Figure 5 presents the transmission probability for the case of almost equal armlengths. It is seen that at equal armlengths, though the transmission probability varies with the wavenumber, only perfect transmission is possible and the reection is never perfect. But at unequal armlengths, perfect reection is also seen to occur. Those dips in the transmission probability can be very sharp. At the limit L1 = L2, those dips vanish by becoming infinitely sharp but not by recovering the transmission from zero. The spectrum does not progressively turn complicated as L2=L1 is detuned from 1. It becomes relatively neat when L2=L1 is a simple rational or commensurate number, where some of the resonant dips collapse. In Fig. 6 we also have plotted out the transmission probability for the case of L2 ≈ 0. The L2 = 0 case is equivalent to a ring touching a wire tangentially, and the transmission is always perfect when there is a SWR (standing wave resonance) in the side-coupled ring, as that is always simultaneously at a perfectly constructive 2PI (two-path interference), like in the L1 = L2 case.

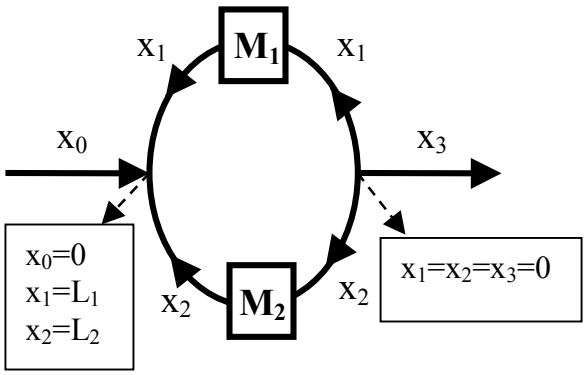

Fig. 4: The generic system we consider has two leads. The boxes on the ring labeled $M_{1,2}$ represent the scatters. A coordinate system x_i is defined for the line segment labeled by i (i=1, 2 and 3). While the arrows denote the increasing direction of the coordinates, the right Y-junction is defined at $x_1 = x_2 = x_3 = 0$, and the left Y-junction is at $x_0=0$, $x_1=L_1$, and $x_2=L_2$.

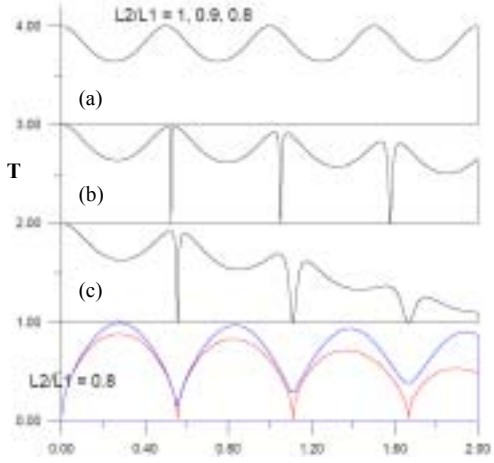

Fig. 5: The transmission probability T is shown versus the dimensionless wave number $kL_1/2\pi$ for clean channels, but different armlength ratios L_1/L_2=(a) 1, (b) 0.9, and (c) 0.8.

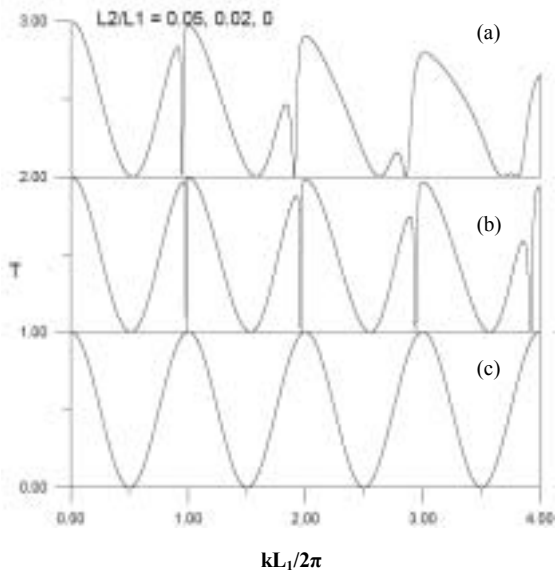

Fig. 6: The transmission probability T is shown versus the dimensionless wave number $kL_1/2\pi$ for clean channels, but different armlength ratios L_1/ L_2=(a) 0.05, (b) 0.02, and (c) 0.

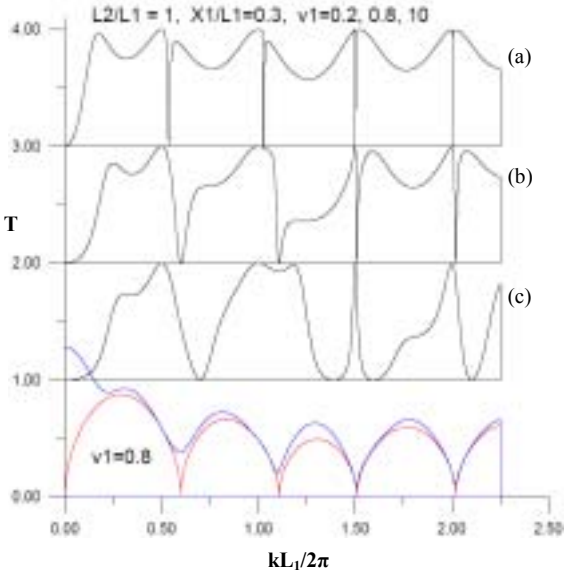

Fig. 7: The transmission probability T is shown versus the dimensionless wave number $kL_1/2\pi$ for $L_1= L_2$ and a point impurity at X_1/ L_1=0.3 with strength v_1=(a) 0.2, (b) 0.8, and (c) 10 (cut-off limit).

B. Single impurity:

Figure 7 shows how the asymmetric Fano-type resonance arises as the strength of the impurity on arm 1 grows. We have chosen L1 = L2 and X1/L1 = 0.3 in Fig. 7.

Such a peakdip line shape resonance is in contrast with the mere dip resonance in the without impurity case in part a., but both of them are seen to develop from zero widths. However small the width of the Fano resonance, it is seen that the peaks always reach one and the dips always reach zero. In Fig. 8 we have shown the transmission probability for the case of the impurity is located near a commensurate location in the ring.

A special commensurate location for the impurity is X1 = 0, i.e., the impurity is right at one of the Y-junctions. Fig. 9 shows the rise of the Fano resonance as the impurity is shifted away from a Y-junction. We have chosen L1 = L2 in Fig. 9. There is no Fano resonance at X1 = 0 since the 2PI process is not disturbed and every SWR occurs at a perfectly constructive 2PI.

c. Double impurity:

Figure 10 shows the transmission probability for symmetric and asymmetric potentials on the arms. For two symmetric point impurities on the arms, i.e., X1 = X2 and impurity-strength v1 = v2 with L1 = L2, only broad peaks due to the SWR in the ring cavity are seen. But when the potentials on the arms are asymmetric, i.e., either one of X1≠X2, v1≠v2, or both equalities are violated , the Fano resonance appears and grows from infinitesimally small width. The perfect or almost-perfect transmission peaks in the Fano resonance are rather surprising since the two leads are separated by the δ-potentials on both arms, and usually one would not expect a perfect transmission at any finite energy, except when there exists intermediate quasibound states such that the Breit-Wigner (BW) resonant tunneling can take place.

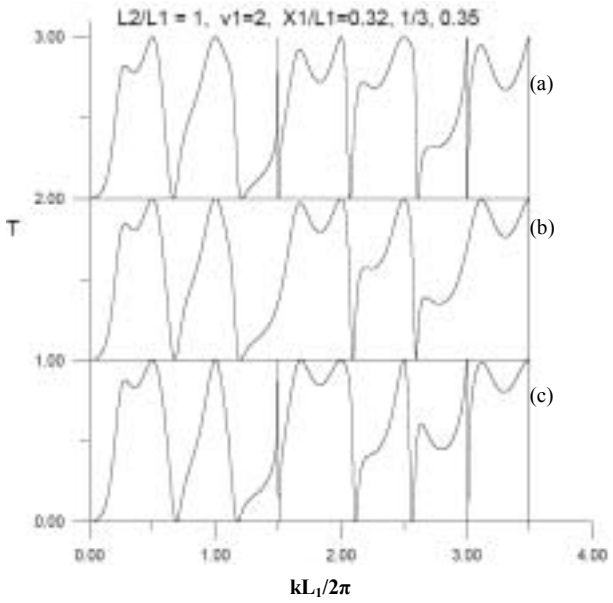

Fig. 8: The transmission probability T is shown versus the dimensionless wave number $kL_1/2\pi$ for $L_1= L_2$ and a point impurity at $v_1=0.2$ with strength X_1/ L_1=(a) 0.32, (b) 1/3, and (c) 0.35. The Fano resonance lines at $kL_1/2\pi \approx 1.5$ and 3 are seen to collapse at the limit $X_1/L_1=1/3$ by shrinking their widths.

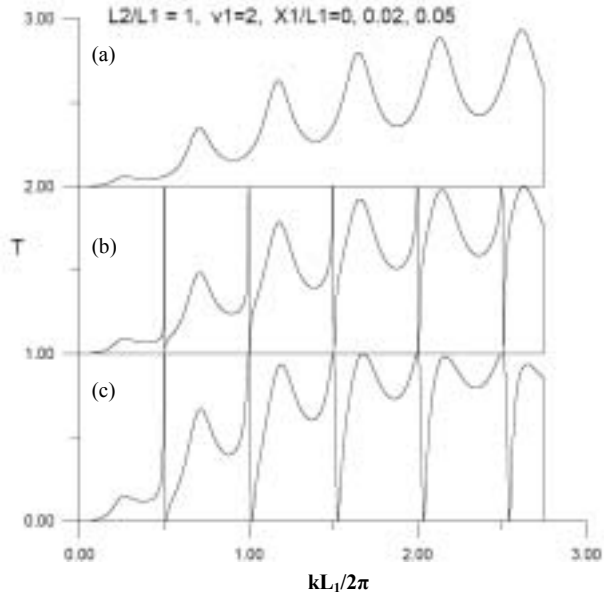

Fig. 9: The transmission probability T is shown versus the dimensionless wave number $kL_1/2\pi$ for $L_1= L_2$ and a point impurity at $v_1=2$ with strength $v_1=2$ at X_1/L_1=(a) 0, (b) 0.02, and (c) 0.05. Fano resonance lines appear and are seen to grow from zero widths when the impurity is shifted away from the symmetry point $X_1=0$.

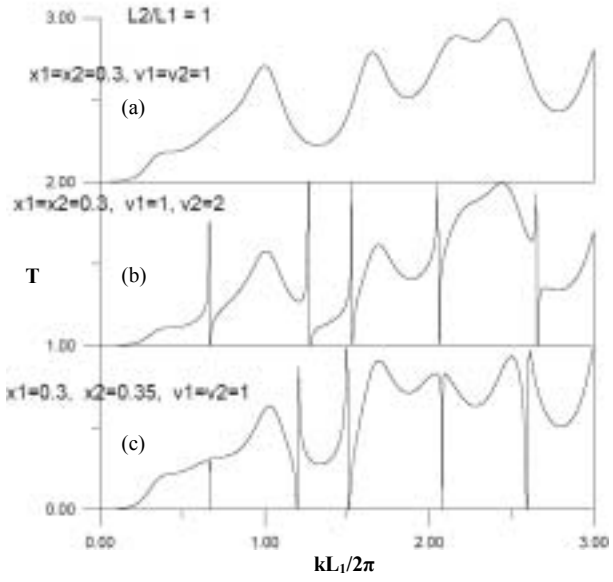

Fig. 10: The transmission probability T is shown versus the dimensionless wave number $kL_1/2\pi$ for $L_1= L_2=L$ and two impurities at $X_{1,2}=2$ with strength $v_{1,2}$.

四、Self-evaluation of project results:

In this project, we have study the quantum transport and spin-dependent transport by applying a time-dependent modulation field. We also discuss the electron in the open dots formed of a quasibound state or true bound state related to its dewell time [68]. The pumping characteristics and mechanisms have been study in adiabatic and nonadiabatic regime [70]. The dephasing phenomena is also investigated in a quantum ring [73]. The spin current generation and detection have been proposed in our paper [69,71]. The new observation of the Fano-structure mechanism is related to standing wave resonance and two-path interference are discussed [73]. Part of these results have been presented in the 2004 annual meeting of the Physical Society of the Republic of China [72]. In all, three papers have been published in Physical Review B [68-70], one paper has been submitted to Physical Review Letters[71], and two papers that are related to quantum ring are in preparation [73].

Appendix A:

PHYSICAL REVIEW B 67, 205324 (2003)

Transport spectroscopy in a time-modulated open quantum dot

C. S. Tang,[1] Y. H. Tan,[2] and C. S. Chu[2]
[1]*Physics Division, National Center for Theoretical Sciences, P.O. Box 2-131, Hsinchu 30013, Taiwan, Republic of China*
[2]*Department of Electrophysics, National Chiao-Tung University, Hsinchu 30010, Taiwan, Republic of China*
(Received 2 October 2002; published 30 May 2003)

We have investigated the time-modulated coherent quantum transport phenomenon in a ballistic open quantum dot. Conductance G and the electron dwell time in the dots are calculated by a time-dependent mode-matching method. Under high-frequency modulation, the traversing electrons are found to exhibit three types of resonant scatterings. They are intersideband scatterings into quasibound states in the dots, into true bound states in the dots, and into quasibound states just beneath the subband threshold in the leads. Dip structures or fano structures in G are their signatures. Our results show structures due to $2\hbar\omega$ intersideband processes. At the above scattering resonances, we have estimated, according to our dwell time calculation, the number of round-trip scatterings which the traversing electrons undertake between the two dot openings.

DOI: 10.1103/PhysRevB.67.205324 PACS number(s): 73.23.−b, 72.30.+q , 72.10.−d

I. INTRODUCTION

In the past decade, the quantum transport phenomenon in open quantum dots has received much attention.[1–11] The open quantum dot, consisting of a submicron sized cavity connecting via point contact leads to two end-electrodes, has become an important device for the investigation of phase-coherent processes and their various mechanisms. The size of the dot and the width of the leads can be controlled by split gates. In high electron mobility samples, and at sufficient low temperatures, the phase-coherent length may well exceed the dimension of the device, allowing electrons to remain coherent while traversing the dot.

Meanwhile, there has been growing interest in the high-frequency responses of mesoscopic nanostructures. The time-modulated fields invoked are either high-frequency electromagnetic fields[12–20] or time-modulated potentials.[21–25] A number of theoretical approaches have been developed to explore quantum transport under such time-modulated fields. The WKB approximation was employed in the study of photovoltaic effect[12] and photon-assisted quantum transport.[13] A mode-matching method was developed for δ-profile[21] as well as finite-range-profile time-modulated potentials.[22] Extension of this method to time-dependent field, represented by a vector potential $\vec{A}(t)$, was carried out by either neglecting[15] or including[18] the contribution of the $\vec{A}(t)^2$ term. This mode-matching method was further extended to accommodate spatial inhomogeneity. The time-modulated field is divided into piecewise potentials connected by either transfer matrices[17] or scattering matrices.[23] Recently, this latter approach has been applied to study a mechanism of nonadiabatic quantum pumping.[25] This pumping mechanism is due to resonances resulting from coherent inelastic scattering, which requires simultaneous changes in both the energy and momentum of the traversing electron, by, respectively, $\hbar\Omega$ and $\hbar K$. Here Ω and K characterize, respectively, the temporal and the spatial variation of the modulation field. Encouraged by the success of the time-modulated mode-matching method, we opt to apply the method to the very interesting case of time-modulated quantum dots.

In the absence of a time-modulated field, transmission of electrons through a quantum dot already shows resonance structures. For the case of a weakly coupled dot—a dot in which electrons are separated from the connecting leads by tunneling barriers—the resonance peaks in the transmission are due to the alignment of the incident electron energy with the quasi-bound-state (QBS) levels in the dot.[26–28] Interestingly, QBS's of a similar nature still exist in the case of an open quantum dot—where tunneling barriers between the dot and the lead are absent. These QBS's, again, give rise to resonances in the transmission. However, dip structures, rather than peaks, become the signatures for the resonances.

When acted upon by a time-modulated potential, the transmission of a weakly coupled dot was found to exhibit additional resonance peaks: peaks associated with ac sidebands.[29] This is due to the alignment, albeit shifted by $n\hbar\omega$, of the incident electron energy with the QBS levels in the dot. Other features found in a time-modulated weakly coupled dot are photon-assisted tunneling,[30] electron pumps,[31] and phase breaking.[32]

Recently, an open quantum dot, acted upon by a transversely polarized electromagnetic field, and connected adiabatically to the connecting leads, has been considered.[33,34] The adiabatic dot-lead connections allow an electron mode in the lead to evolve into an electron mode in the dot. Thus, situations occur when an electron in the lower mode in the dot can exit the dot without reflection, while an electron at the same energy, but in a higher mode in the dot, is trapped inside it. As such, intermode transitions between the above two modes in the dot, as induced by the transversely polarized electromagnetic field, were found to lead to giant mesoscopic conductance fluctuations[33] and microwave-induced resonant blocking in a mesoscopic channel.[34]

The adiabaticity of the dot-lead connection holds for large quantum dots. But, as the sizes of the open quantum dot shrink and approach the realm of the Fermi wavelength, the dot-lead connections can no longer remain adiabatic. More recent experimental findings in dc transport in open quantum dots—that transport occurs through individual eigenstates of the corresponding closed dot,[35] and that the conductance oscillations correlate to the recurrence of specific groups of

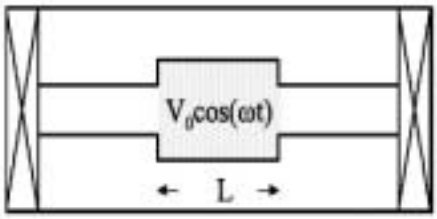

FIG. 1. Schematic illustration of an open quantum dot that is acted upon by a gate-induced time modulation with two leads connecting adiabatically to two end electrodes.

wave function scars in the dot[10]—indicate unequivocally that intermode scattering and backscattering are present, respectively, at the dot-lead connections. The effect of impurity should play no role here because of the high mobility of the sample used in these experiments.

Therefore, in this work, we consider a time-modulated open quantum dot with nonadiabatic dot-lead connections. We calculate the dc conductance G of a time-modulated open quantum dot and the dwell time τ_d of the traversing electron in the dot. We have analyzed the resonance structures in G associated with the time modulation and are able to categorize them according to their respective dynamical processes involved. Of these three resonance types, one is analogous to that found in time-modulated weakly coupled dots. It is associated with the alignment of the incident electron energy with that of the ac sidebands of the QBS's inside the open dot. The second type is associated with the coherent inelastic scattering of the traversing electron into the true bound state in the open dot—bound state whose energy is lower than the threshold energy of the leads. The third type of resonance structures is most unexpected. It is associated with the coherent inelastic scattering of the traversing electron into the QBS in the lead—with energy just beneath the threshold energy of the lead. Also, from the dwell time τ_d, we estimate the number of scatterings that occur in the dot as the resonance structures establish themselves. In all, our results demonstrate the potential of establishing quantum transport as a spectroscopic probe for the QBSs and true bound states in the open dot—and possibly in other mesoscopic structures—through the coupling of a time-modulated field to the system.

In Sec. II, we present our theoretical method for the calculation of G and τ_d. The numerical results are presented and discussed in Sec. III. Finally, in Sec. IV, we present our conclusions.

II. MODEL AND METHOD

The system under investigation is sketched (top view) in Fig. 1, where the shaded area denotes the region acted upon by a time-modulated potential. The dot we consider has physical parameters typical to that in high mobility two-dimensional electron gas, formed in an AlGaAs-GaAs heterostructure. As such, mobility $\mu_e \sim 10^6$ cm^2/V s, mean free path $l \sim 1$ μm at sufficient low temperatures, and dots with submicron dot sizes would be in the ballistic regime. The Hamiltonian is given by

$$H = -\frac{\hbar^2}{2m}\left[\frac{\partial^2}{\partial x^2}+\frac{\partial^2}{\partial y^2}\right] + V_c(x,y) + V(x,t), \qquad (1)$$

where $V_c(x,y)$ is the confinement potential, chosen to be of hard-wall type, that defines the dot and the leads. It is given by $V_c=0$ if $|y|<W_1/2$ and $|x|>L/2$; $V_c=0$ if $|y|<W_2/2$ and $|x|<L/2$; and $V_c=\infty$ if otherwise. Here W_1, W_2 are, respectively, widths of the lead and the dot. The time-modulated potential

$$V(x,t) = V_0\cos(\omega t)\Theta(L/2-|x|)$$

acts only upon the dot.

For the sake of convenience, the physical quantities that appear in the following equations are dimensionless: with energy unit $E^* = E_F = \hbar^2 k_F^2/2m$, wave vector unit $k^* = k_F$, length unit $a^* = 1/k_F$, time unit $t^* = \hbar/E_F$, and frequency unit $\omega^* = 1/t^*$. The scattering wave function for an electron incident upon the dot from the lth channel in the left lead is of the form

$$\psi_l(x,y,t) = \chi_l(y)e^{ik_l(0)x}e^{-i\mu t} + \sum_{n'}\sum_{m'}\chi_{n'}(y)r_{n'l}(m')\times\exp[-ik_{n'}(m')x - i(\mu+m'\omega)t]$$

$$\text{if } x<-L/2,$$

$$\psi_l(x,y,t) = \sum_{k'}\phi_{k'}(y)\int d\epsilon[\tilde{A}_{k'l}(\epsilon)e^{i\beta_{k'}(\epsilon)x} + \tilde{B}_{k'l}(\epsilon)e^{-i\beta_{k'}(\epsilon)x}]\times\exp\left[-i\epsilon t - i\frac{V_0}{\omega}\sin\omega t\right] \quad \text{if } |x|<L/2, \qquad (2)$$

$$\psi_l(x,y,t) = \sum_{n'}\sum_{m'}\chi_{n'}(y)t_{n'l}(m')\exp[ik_{n'}(m')x - i(\mu+m'\omega)t] \quad \text{if } x>L/2,$$

where the subscripts n' and k' are the subband indices in, respectively, the leads and the dot, and m' is the sideband index. In addition, $k_l(m') = [\mu+m'\omega-(l\pi/W_1)^2]^{1/2}$ and $\beta_{k'}(m') = [\mu+m'\omega-(k'\pi/W_2)^2]^{1/2}$ denote, respectively, the wave vectors in the lead and the dot. The normalized transverse subband states are $\chi_l(y) = (2/W_1)^{1/2}\sin[l\pi(y/W_1+1/2)]$ and $\phi_{k'}(y) = (2/W_2)^{1/2}\sin[k'\pi(y/W_2+1/2)]$.

The matching of the wave functions at the openings of the dot, and at all times, requires the coefficients in the dot to have the form

$$\tilde{\mathcal{F}}_{k'l}(\epsilon) = \sum_{m'}\mathcal{F}_{k'l}(m')\delta(\epsilon-\mu-m'\omega),$$

where $\tilde{\mathcal{F}}_{k'l}(\epsilon)$ refers to either $\tilde{A}_{k'l}(\epsilon)$ or $\tilde{B}_{k'l}(\epsilon)$. Performing the matching, and after some algebra, we obtain

$$\left[A_{kl}(m)\exp\left(-i\beta_k(m)\frac{L}{2}\right)+B_{kl}(m)\exp\left(i\beta_k(m)\frac{L}{2}\right)\right]$$
$$=\sum_{n'}\sum_{m'}J_{m'-m}\left(\frac{V_0}{\omega}\right)\left[a_{lk}\exp\left(-ik_l(m')\frac{L}{2}\right)\delta_{n'l}\delta_{m'0}+a_{n'k}r_{n'l}(m')\exp\left(ik_{n'}(m')\frac{L}{2}\right)\right], \quad (3)$$

$$\left[A_{kl}(m)\exp\left(i\beta_k(m)\frac{L}{2}\right)+B_{kl}(m)\exp\left(-i\beta_k(m)\frac{L}{2}\right)\right]$$
$$=\sum_{n'}\sum_{m'}J_{m'-m}\left(\frac{V_0}{\omega}\right)\left[a_{n'k}t_{n'l}(m')\exp\left(ik_{n'}(m')\frac{L}{2}\right)\right], \quad (4)$$

$$\sum_{k'}a_{nk'}\beta_{k'}(m)\left[A_{k'l}(m)\exp\left(-i\beta_{k'}(m)\frac{L}{2}\right)-B_{k'l}(m)\exp\left(i\beta_{k'}(m)\frac{L}{2}\right)\right]$$
$$=\sum_{m'}J_{m'-m}\left(\frac{V_0}{\omega}\right)k_n(m')\left[\delta_{nl}\delta_{m'0}\exp\left(-ik_l(m')\frac{L}{2}\right)-r_{nl}(m')\exp\left(ik_{n'}(m')\frac{L}{2}\right)\right], \quad (5)$$

and

$$\sum_{k'}a_{nk'}\beta_{k'}(m)\left[A_{k'l}(m)\exp\left(i\beta_{k'}(m)\frac{L}{2}\right)-B_{k'l}(m)\exp\left(-i\beta_{k'}(m)\frac{L}{2}\right)\right]$$
$$=\sum_{m'}J_{m'-m}\left(\frac{V_0}{\omega}\right)k_n(m')t_{nl}(m')\exp\left(ik_n(m')\frac{L}{2}\right), \quad (6)$$

where Eqs. (5) and (6) are obtained from matching the derivatives of the wave functions. The overlapping integral a_{lk} of the transverse subband states is given by

$$a_{lk}=\int_{-W_1/2}^{W_1/2}\chi_l(y)\phi_k(y)dy \quad (7)$$

and the identity $\exp(iz\sin\omega t)=\sum_p J_p(z)\exp(ip\omega t)$ has been invoked. We have solved Eqs. (3)–(6) for the coefficients $A_{kl}(m)$, $B_{kl}(m)$, $r_{n'l}(m')$ and $t_{n'l}(m')$. Furthermore, we note that the sole appearance of V_0 in Eqs. (3)–(6) is in the form V_0/ω and as an argument of the Bessel functions J_m. This shows a general trend that the effect of the time-modulated potential decreases with the raising of the frequency ω.

In the low drain-source bias regime, the dc conductance is given by

$$G=\frac{2e^2}{h}\sum_{l=1}^{N}T_l, \quad (8)$$

where N denotes the number of propagating channels in the leads. The current transmission coefficient T_l for an electron incident from the lth channel in the lead is

$$T_l=\sum_{n'}\sum_{m'}\frac{k_{n'}(m')}{k_l(0)}|t_{n'l}(m')|^2. \quad (9)$$

The current reflection coefficient R_l has a similar form and the current conservation condition $T_l+R_l=1$ is used to check on our numerical accuracy.

The stationary dwell time within one-dimensional system was well defined.[36] However, in a multichannel system, such as open quantum dots, we should consider not only the probability of finding the particle in the dot, but also that due to evanescent states in the vicinity of the dot. Hence, we define the dwell time as

$$\tau_d=\frac{\int\int_{\mathcal{A}'}\langle|\psi(x,y,t)|^2\rangle_{\text{t.a.}}dxdy}{\int dy j_{\text{inc}}}, \quad (10)$$

where j_{inc} denotes the incident electron flux. The subscript t.a. denotes time average. Here we note that the integral in the numerator and its region of interest $\mathcal{A}'$ include not only the region inside the quantum dot (region II), but also the evanescent modes on both the left-hand side (region I) and the right-hand side (region III) of the dot. Hence, the time-averaged probability density in the numerator of Eq. (10) can be separated into three integrals, expressed explicitly as

$$\int\int_{\text{I}}dxdy\langle|\psi(x,y,t)|^2\rangle_{\text{t.a.}}=\int_{-\infty}^{-L/2}dx\sum_{n'}\sum_{m'}|r_{n'l}(m')|^2e^{2\kappa_{n'}(m')x}, \quad (11)$$

$$\int\int_{\text{II}}dxdy\langle|\psi(x,y,t)|^2\rangle_{\text{t.a.}}=\int_{-L/2}^{L/2}dx\sum_{k'}\sum_{m'}\{A_{k'l}(m')A^*_{k'l}(m')\exp[i(\beta_{k'}(m')-\beta^*_{k'}(m'))x]$$
$$+B_{k'l}(m')B^*_{k'l}(m')e^{-i(\beta_{k'}(m')-\beta^*_{k'}(m'))x}+2\text{Re}[A_{k'l}(m')B^*_{k'l}(m')e^{i(\beta_{k'}(m')+\beta^*_{k'}(m'))x}]\}, \quad (12)$$

and

$$\int\int_{\text{III}} dxdy\langle|\phi(x,y,t)|^2\rangle_{\text{t.a.}} = \int_{L/2}^{\infty} dx \sum_{n'} \sum_{m'} |t_{n'i}(m')|^2 \exp[-2\kappa_{n'}(m')x], \tag{13}$$

where the indices n' and m' in the summation for regions I and III include only the evanescent waves, and $\kappa_{n'}(m) = -ik_{n'}(m)$. Substituting Eqs. (11)–(13) into Eq. (10), we obtain the average dwell time of electrons in the open quantum dot system.

III. RESULTS AND DISCUSSION

In this section, we present our numerical examples for exploring the time-modulated effects on the quantum transport in open quantum dots—the conductance and the dwell time versus the incident electron energy μ. In the following, we choose energy unit $E^*=9$ meV, length unit $a^*=8$ nm, unit of angular frequency $\omega^*=13.6$ Trad/s, and the effective mass $m^*=0.067m_e$, where m_e is the free electron mass of an electron. The geometric parameters are chosen such that the width $W_1=10(=80$ nm) for the leads, and the width $W_2=20(=160$ nm) and the length $L=30(=240$ nm) for the open quantum dot, which is typical for current experimental fabrication. It is convenient to define $X^2=\mu/\varepsilon_1$ where $\varepsilon_1=(\pi/W_1)^2$ is the first transverse subband level in the leads. Then the integral values of X stand for the number of occupied subbands in the leads.

In the absence of time modulation, the quantum states of the open quantum dot associate closely with the bound states of the corresponding closed dot with the same geometry. For a closed dot with length L and width W_2, the bound-state energy $E_{\text{b.s.}}=(n_x\pi/L)^2+(n_y\pi/W_2)^2$ is labeled by a pair of quantum number (n_x,n_y). Then we may obtain the rescaled bound-state levels $\underline{E}(n_x,n_y)=E_{\text{b.s.}}/\varepsilon_1=n_x^2/9+n_y^2/4$ inside the closed dot. For an open dot, the energy spectrum consists of both true bound states and QBS's corresponding either to electrons with energy μ less than or higher than the threshold energy ε_1 in the lead. As such, there are only two possible true bound states in the open dot: $E_{B1}\simeq\underline{E}(1,1)=0.361$ and $E_{B2}\simeq\underline{E}(2,1)=0.694$.

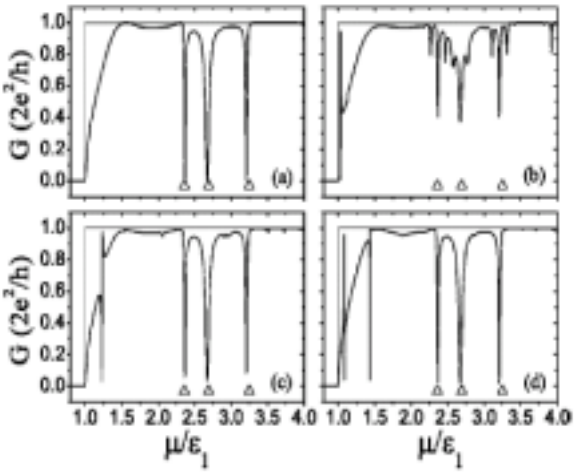

FIG. 2. Energy dependence of the quantum dot conductance G in the lowest subband as a function of incident electron energy μ, in units of ε_1, for cases of (a) no external modulation, (b)–(d) modulation amplitude $V_0=0.1\varepsilon_1$, with angular frequencies (b) $\omega=0.1\varepsilon_1$, (c) $0.3\varepsilon_1$, and (d) $0.5\varepsilon_1$.

In Fig. 2, the conductance characteristic is studied as a function of incident electron energy: (a) in the absence of time modulation, as a comparative reference and (b)–(d) in the presence of time modulation with angular frequencies $\omega/\varepsilon_1=0.1$, 0.3, and 0.5, respectively, which also correspond to frequencies $f=\omega/2\pi\simeq21.4$, 64.2, and 107 GHz. This frequency range is typical for current experiments.[37] In addition, the modulation amplitude is chosen to be $V_0=0.1\varepsilon_1$ ($\simeq0.09$ meV). There are three dip structures common to all four plots. These dip structures occur at energies $\mu/\varepsilon_1=2.364(E_{Q1})$, $2.672(E_{Q2})$, and $3.208(E_{Q3})$. These are associated with the alignment of the incident electron energy with that of the QBS levels inside the open dot, as is indicated by the open triangle symbols locating the closed dot $\underline{E}(1,3)=2.361$, $\underline{E}(2,3)=2.694$, and $\underline{E}(3,3)=3.250$. The corresponding dwell time of these QBSs are, respectively, $\tau_d\simeq73.5$, 26.7, and 69.0 ps, as shown in Fig. 3(a). These dwell time peak structures confirm the resonant nature of the states inside the dot.

Another interesting feature in Fig. 2(b) are the side-dip structures around the QBS's E_{Qi}, which are associated with electrons at incident energy μ that are able to make m-photon intersideband transitions into the ith QBS level. The condition is

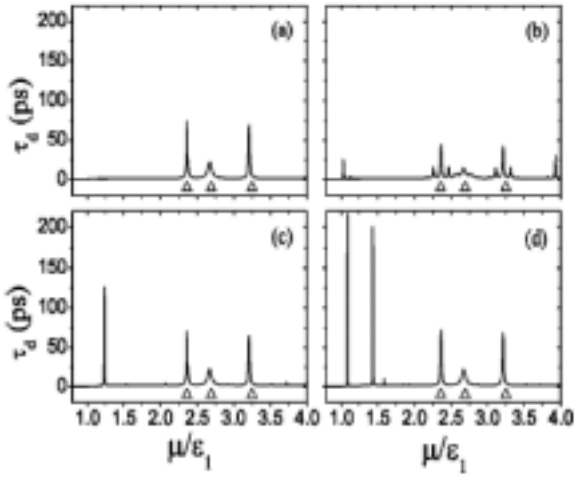

FIG. 3. The dwell time τ_d of the traversing electron is plotted as a function of the incident electron energy μ in units of ε_1. The parameters are the same as in Figs. 2(a)–2(d).

$$\mu + m\hbar\omega = E_{Qi}, \tag{14}$$

where the positive m and negative m indicate, respectively, the absorption and emission of m photons. Hence $m=-1$ side dips are at $\mu/\varepsilon_1=2.465$, 2.770, 3.309; $m=+1$ side dips are at $\mu/\varepsilon_1=2.165$, 2.574, 3.110; and $m=+2$ side dips are at $\mu/\varepsilon_1=2.266$, 3.008. The $m=-2$ process in the vicinity of the E_{Q3} state is barely identified and is at $\mu/\varepsilon_1=3.411$.

Two additional types of intersideband transition mechanisms are found in the low-energy regime in Fig. 2. As is shown in Fig. 2(d), where the frequency $\omega=0.5\varepsilon_1$ is high enough, the electrons with $\mu/\varepsilon_1=1.087$ may emit $\hbar\omega$ and make transitions into E_{B2}—the true bound state in the dot. The electron dwell time of this structure is $\tau_d\cong 216.6$ ps, see Fig. 3(d). In addition, electrons may also emit photons to make transitions into a QBS formed at energy just beneath a subband threshold in the lead. This mechanism is identified to be the fano structures at $\mu/\varepsilon_1=1.028$, 1.233, and 1.435, as shown in Figs. 2(b)–2(d), respectively, where $(\mu-\omega)/\varepsilon_1$ is close to 1 from below. Correspondingly, the dwell times of these structures are $\tau_d\simeq 23.0$, 125.5, and 200.2 ps, see Figs. 3(b)–3(d). More precisely, these structures correspond to electrons that emit $\hbar\omega$ to $\mu/\varepsilon_1=0.93$ and are trapped temporarily to form QBS's in the lead.

To provide further evidence for the above two transition mechanisms, we plot, in Fig. 4, the spatial dependence of the time-averaged probability density. The parameters are chosen to be the same as in Fig. 2(d). When the electron incident at energy $\mu=1.0854\varepsilon_1$, as shown in Fig. 4(a), we see that the time-averaged electron probability concentrates entirely within the dot and is like a (2,1) state. This supports the fact that the electron is trapped in a true bound state in the dot. Second, when the electron incident at energy $\mu=1.4353\varepsilon_1$, the electron probability has long exponential tails extending into the leads. The edges of the dot are at $x=\pm 15$. This demonstrates that the electron has made an intersideband transition, by emitting one photon, into a QBS in the lead whose energy is just below the threshold energy. We have also checked that a similar process can be found even in a time-modulated one-dimensional quantum well connecting to leads. A traversing electron can make intersideband transitions to QBS's in the leads or to true bound states in the well.[38]

To better appreciate the meaning of the dwell time, we define the number of round-trip scatterings, N_{sc}, undertaken by the traversing electron. It is the ratio of the dwell time τ_d to the ballistic time τ_b the electron takes to go between the two dot-openings. The ballistic time for electrons traversing through the quantum dot is simply $\tau_b\sim L/v_e$, where v_e denotes the electron velocity and is given by $v_e=\hbar k_x/m$. We consider the electron incident in the lowest subband and then the electron ballistic time is given by $\tau_b=L/(\mu-\varepsilon_1)^{1/2}$ in units of t^*. Hence, in Fig. 3(d), the main peaks at $\mu/\varepsilon_1=1.085$, 1.435, 2.365, 2.673, and 3.210 correspond to the ballistic times $\tau_b\simeq 24.0$, 16.1, 6.01, 5.43, and 4.72 ps, respectively. The corresponding τ_d's are, respectively, 216.6, 200.2, 71.8, 21.8, and 67.9. Therefore, we obtain the number of round-trip scatterings, $N_{sc}\equiv\tau_d/2\tau_b\sim 4.5$, 6.2, 6.0, 2.0, and 7.2, respectively. In light of the above analysis, we can see that two round-trip times are already sufficient to form a significant QBS level inside the open dot. The estimation for τ_b could be improved by considering the effective electron velocity in the dot, rather than in the lead. But we expect N_{sc} to remain of the same order of magnitude as shown here. Moreover, the N_{sc} obtained here is the lower bound to any such improved estimation.

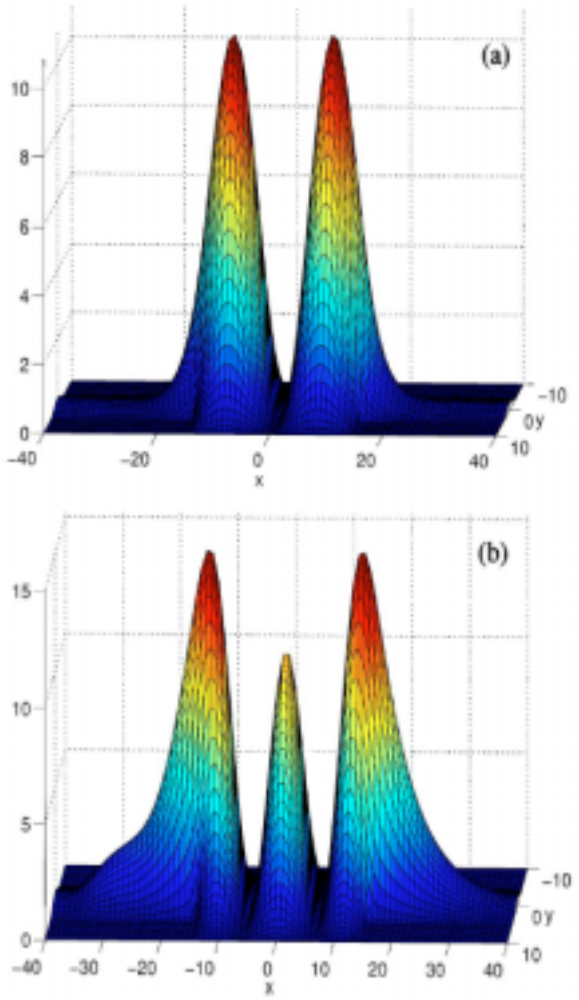

FIG. 4. (color online). The spatial dependence of the time-averaged electron probability density: (a) $\mu=1.0854\varepsilon_1$ and (b) $\mu=1.4353\varepsilon_1$. Other parameters are the same as in Fig. 2(d). The edges of the dot are at $L=\pm 15$.

It is known[22] that the strength of the time-modulated potential depends on the ratio of V_0 to ω. As a result, for a given amplitude V_0, the sideband dip features are suppressed with increase in the modulation frequency ω. This is illustrated in Figs. 2(c) and 2(d). On the other hand, if we fix $V_0/\omega=1$ in Fig. 5, and choose the modulation amplitude to be $V_0/\varepsilon_1=0.05$, 0.1, and 0.2 for Figs. 5(a)–5(c), respectively, we can see the side dips due to $2\hbar\omega$ intersideband processes in all the figures. This assures us that V_0/ω is an important index for photon absorption and emission processes. Furthermore, the QBS levels that associate with a fewer number of round-trip scatterings may be merged with its nearby sidebands, formang a broadened dip structure: such as the wide-dip structure at $\mu/\varepsilon_1=2.672$ in Fig. 5(a). In the

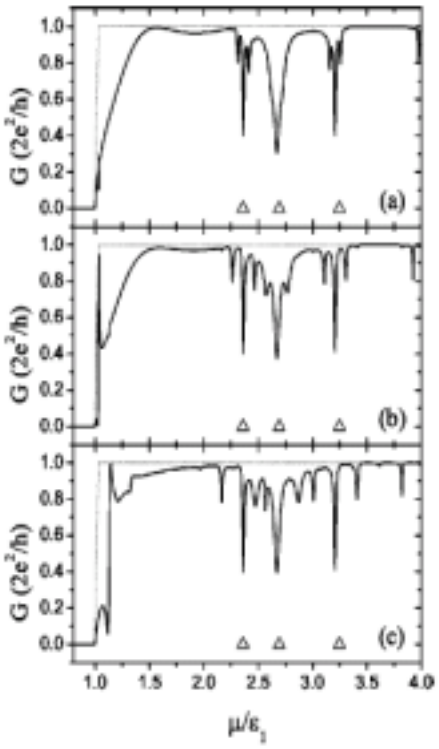

FIG. 5. Conductance is plotted as a function of electron energy μ for a fixed $V_0/\omega = 1.0$. The values of V_0 (or ω) are (a) $0.05\varepsilon_1$, (b) $0.1\varepsilon_1$, and (c) $0.2\varepsilon_1$, respectively.

low-energy regime, again, electrons are able to undertake one-photon (or two-photon) emission processes into a subband threshold in the lead. This one-(or two-)photon mechanism is demonstrated by small dip structures in G at $\mu/\varepsilon_1 = 1.024$ (or 1.129) in Fig. 5(b) and $\mu/\varepsilon_1 = 1.118$ (or 1.317) in Fig. 5(c).

To conclude this section, we note in passing that despite of wide dot openings, electrons traversing through the dot are still effectively mediated by just a few bound states of the corresponding closed dot structure. Our results show that the conductance spectra for a time-modulated open dot show more intersideband structures than those associated with the bound states of the corresponding close dot. We believe that these mechanisms should find their way of manifestation in the time-modulated phenomena of other nanostructures.

IV. CONCLUSIONS

In this work we have extended the time-dependent mode matching approach to the study of quantum transport in open quantum dot systems. We have calculated the conductance, the dwell time, and the spatial distribution of the electron probability and their dependence on the modulation amplitudes and frequencies.

In conclusion, we have shown three types of coherent inelastic scatterings in a time-modulated open quantum dot. We have demonstrated the potential of establishing quantum transport as a spectroscopic probe for the QBS's and true bound states in an open dot through the coupling of a time-modulated field to the system.

ACKNOWLEDGMENTS

The authors wish to acknowledge the National Science Council of the Republic of China for financially supporting this research under Grants Nos. NSC90(91)-2119-M-007-004 (NCTS), NSC90-2112-M-262-001 (CST), and NSC90-2112-M-009-044 (CSC). Computational facilities supported by the National Center for High-Performance Computing are gratefully acknowledged.

[1] C.M. Marcus, A.J. Rimberg, R.M. Wetervelt, P.F. Hopkins, and A.C. Gossard, Phys. Rev. Lett. **69**, 506 (1992).
[2] A.M. Chang, H.U. Baranger, L.N. Pfeiffer, and K.W. West, Phys. Rev. Lett. **73**, 2111 (1994).
[3] H.I. Chan, R.M. Clarke, C.M. Marcus, K. Campman, and A.C. Gossard, Phys. Rev. Lett. **74**, 3876 (1995).
[4] M. Persson, J. Pettersson, B. von Sydow, P.E. Lindelof, A. Kristensen, and K.-F. Berggren, Phys. Rev. B **52**, 8921 (1995).
[5] M.W. Keller, A. Mittal, J.W. Sleight, R.G. Wheeler, D.E. Prober, R.N. Sacks, and H. Shtrikmann, Phys. Rev. B **53**, R1693 (1996).
[6] Y. Wang, N. Zhu, and J. Wang, Phys. Rev. B **53**, 16 408 (1996).
[7] R. Akis, D.K. Ferry, and J.P. Bird, Phys. Rev. Lett. **79**, 123 (1997).
[8] I.V. Zozoulenko and T. Lundberg, Phys. Rev. Lett. **81**, 1744 (1998).
[9] R. Akis, D.K. Ferry, and J.P. Bird, Phys. Rev. Lett. **81**, 1745 (1998).
[10] J.P. Bird, R. Akis, D.K. Ferry, D. Vasileska, J. Cooper, Y. Aoyagi, and T. Sugano, Phys. Rev. Lett. **82**, 4691 (1999).
[11] A.P.S. de Moura, Y.-C. Lai, R. Akis, J.P. Bird, and D.K. Ferry, Phys. Rev. Lett. **88**, 236804 (2002).
[12] F. Hekking and Y.V. Nazarov, Phys. Rev. B **44**, 11 506 (1991).
[13] S. Feng and Q. Hu, Phys. Rev. B **48**, 5354 (1993).
[14] L.Y. Gorelik, A. Grincwajg, V.Z. Kleiner, R.I. Shekhter, and M. Jonson, Phys. Rev. Lett. **73**, 2260 (1994).
[15] F.A. Maaø and L.Y. Gorelik, Phys. Rev. B **53**, 15 885 (1996).
[16] C.S. Chu and C.S. Tang, Solid State Commun. **97**, 119 (1996).
[17] M. Wagner and W. Zwerger, Phys. Rev. B **55**, R10 217 (1997).
[18] C.S. Tang and C.S. Chu, Phys. Rev. B **60**, 1830 (1999).
[19] Wenjun Li and L.E. Reichl, Phys. Rev. B **62**, 8269 (2000).
[20] C.S. Tang and C.S. Chu, Physica B **292**, 127 (2000).
[21] P.F. Bagwell and R.K. Lake, Phys. Rev. B **46**, 15 329 (1992).
[22] C.S. Tang and C.S. Chu, Phys. Rev. B **53**, 4838 (1996).
[23] C.S. Tang and C.S. Chu, Physica B **254**, 178 (1998).
[24] Wenjun Li and L.E. Reichl, Phys. Rev. B **60**, 15 732 (1999).
[25] C.S. Tang and C.S. Chu, Solid State Commun. **120**, 353 (2001).
[26] J. Wang and H. Guo, Appl. Phys. Lett. **60**, 654 (1992).
[27] S. Tarucha, D.G. Austing, T. Honda, R.J. van der Hage, and L.P. Kouwenhoven, Phys. Rev. Lett. **77**, 3613 (1996).

[28] L.P. Kouwenhoven *et al.*, in *Mesoscopic Electron Transport, Vol. 345 of Proceeding of a NATO Advanced Studies Institute, Series E: Applied Sciences*, edited by L.L. Sohn, L.P. Kouwenhoven, and G. Schön (Kluwer, Dordrecht, 1997).

[29] T.H. Oosterkamp, L.P. Kouwenhoven, A.E.A. Kooten, N.C. van der Vaart, and C.J.P.M. Harmans, Phys. Rev. Lett. **78**, 1536 (1997).

[30] T. Christen and M. Büttiker, Phys. Rev. B **53**, 2064 (1996).

[31] L.J. Geerlings, V.F. Anderegg, P.A.M. Holweg, J.E. Mooij, H. Pothier, D. Esteve, C. Urbina, and M.H. Devoret, Phys. Rev. Lett. **64**, 2691 (1990).

[32] M.P. Anantram and S. Datta, Phys. Rev. B **51**, 7632 (1995).

[33] L.Y. Gorelik, F.A. Maaø, R.I. Shekhter, and M. Jonson, Phys. Rev. Lett. **78**, 3169 (1997).

[34] S. Blom and L.Y. Gorelik, Phys. Rev. B **64**, 045320 (2001).

[35] I.V. Zozoulenko, A.S. Sachrajda, C. Gould, K.-F. Berggren, P. Zawadzki, Y. Feng, and Z. Wasilewski, Phys. Rev. Lett. **83**, 1838 (1999).

[36] F.T. Smith, Phys. Rev. **118**, 349 (1960).

[37] H. Qin, F. Simmel, R.H. Blick, J.P. Kotthaus, W. Wegscheider, and M. Bichler, Phys. Rev. B **63**, 035320 (2001).

[38] C.S. Tang and C.S. Chu (unpublished).

Appendix B:

PHYSICAL REVIEW B 68, 233307 (2003)

Spin-current generation and detection in the presence of an ac gate

A. G. Mal'shukov,[1] C. S. Tang,[2] C. S. Chu,[3] and K. A. Chao[4]
[1]Institute of Spectroscopy, Russian Academy of Science, 142190, Troitsk, Moscow oblast, Russia
[2]Physics Division, National Center for Theoretical Sciences, P.O. Box 2-131, Hsinchu 30013, Taiwan
[3]Department of Electrophysics, National Chiao-Tung University, Hsinchu 30010, Taiwan
[4]Solid State Theory Division, Department of Physics, Lund University, S-22362 Lund, Sweden
(Received 15 August 2003; published 24 December 2003)

We predict that in a narrow gap III-V semiconductor quantum well or quantum wire, an observable electron spin current can be generated with a time-dependent gate to modify the Rashba spin-orbit coupling constant. Methods to rectify the so generated ac current are discussed. An all-electric method of spin-current detection is suggested, which measures the voltage on the gate in the vicinity of a two-dimensional electron gas carrying a time-dependent spin current. Both the generation and detection do not involve any optical or magnetic mediator.

DOI: 10.1103/PhysRevB.68.233307 PACS number(s): 73.63.−b, 71.70.Ej, 72.25.Dc

One key issue in spintronics based on semiconductor is the efficient control of the spin degrees of freedom. Datta and Das[1] suggested the use of gate voltage to control the strength of Rashba spin-orbit interaction (SOI)[2] which is strong in narrow gap semiconductor heterostructures. In InAs-based quantum wells a variation of 50% of the SOI coupling constant was observed experimentally.[3,4] Consequently, much interest has been attracted to the realization of spin-polarized transistors and other devices based on using electric gate to control the spin-dependent transport.[5]

In addition to using a static gate to control the SOI strength and so control the stationary spin transport, new physical phenomena can be observed in time-dependent spin transport under the influence of a fast varying gate voltage. Along this line, in this article we will consider a mechanism of ac spin current generation using time-dependent gate. This mechanism employs a simple fact that the time variation of Rashba SOI creates a force which acts on opposite spin electrons in opposite directions. Inversely, when a gate is coupled to a nearby electron gas, the spin current in this electron gas also induces a variation of the gate voltage, and hence affects the electric current in the gate circuit. We will use a simple model to clarify the principle of such a new detection mechanism without any optical or magnetic mediator. The systems to be studied will be 1D electron gas in a semiconductor quantum wire (QWR) and 2D electron gas in a semiconductor quantum well (QW).

We consider a model in which the Rashba SOI is described by the time-dependent Hamiltonian $H_{SO}(t)=\hbar\alpha(t)\times(\vec{k}\times\vec{\nu})\cdot\vec{s}$, where $\vec{k}$ is the wave vector of an electron, $\hbar\vec{s}$ is the spin operator, and $\vec{\nu}$ is the unit vector. For a QWR $\vec{\nu}$ is perpendicular to the wire axis, and for a QW perpendicular to the interfaces. The time dependence of the coupling parameter $\alpha(t)$ is caused by a time-dependent gate.[6] To explain clearly the physical mechanisms leading to the spin-current generation, we will first consider the 1D electron gas in a QWR, and assume $\alpha(t)$ to be a constant α for $t<0$, and $\alpha(t)=0$ for $t>0$. For the 1D system we choose the x direction as the QWR axis and y axis parallel to $\vec{\nu}$, to write the SOI coupling in the form $H_{SO}(t)=\hbar\alpha(t)k_x s_z$. For $t<0$ the spin degeneracy of conduction electrons is lifted by SOI, producing a splitting $\Delta=\hbar\alpha k_x$ between $s_z=1/2$ and $s_z=-1/2$ bands, as shown in Fig. 1 by solid curves together with the Fermi energy E_F. The spin current in this state is zero, as it should be under thermal equilibrium.

Indeed, the spin current is defined as $I_z(t)=I_\uparrow(t)-I_\downarrow(t)$, where $I_\uparrow(t)$ [or $I_\downarrow(t)$] is the partial current associated with the spin projections $s_z=1/2$ (or $s_z=-1/2$). Hence,

$$I_z(t)=\frac{\hbar}{2L}\sum_{E(k_x)<E_F}[v_\uparrow(k_x)-v_\downarrow(k_x)], \tag{1}$$

where L is the length of the QWR. Taking the momentum derivative of the Hamiltonian, we obtain the velocity as

$$v_{\uparrow,\downarrow}(k_x)=\hbar k_x/m^*\pm\alpha(t)/2. \tag{2}$$

The spin current is then readily obtained as

$$I_z(t)=(\hbar n/4m^*)(\hbar k_\uparrow-\hbar k_\downarrow)+\hbar\alpha(t)n/4, \tag{3}$$

where n is the 1D electron density, and $k_\uparrow$ (or $k_\downarrow$) is the average momentum in the $\uparrow$-spin (or $\downarrow$-spin) band.

For a parabolic band $\hbar k_\uparrow=-m^*\alpha/2$ and $\hbar k_\downarrow=m^*\alpha/2$. Although $\hbar k_\uparrow-\hbar k_\downarrow$ gives a finite contribution to $I_z(t)$ in Eq. (3), for $t<0$ where $\alpha(t)=\alpha$, this contribution is compensated by the contribution $\hbar\alpha n/4$ due to the SOI. Hence, the total spin current $I_z(t)=0$ for $t<0$. However, when the SOI is switched off at $t=0$, $\alpha(t)=0$ and so the spin current is finite, because the average electron momenta retain the same as they were at $t<0$. As time goes on, the electron momenta relax with a relaxation time τ. Therefore, $I_z(t)=-(\hbar\alpha n/4)\exp(-t/\tau)$ for $t>0$.

It is instructive to make a Fourier transform of $I_z(t)$ to obtain a Drude-like expression

$$I_z(\Omega)=\left[\frac{\tau\hbar n}{2m^*(i\Omega\tau-1)}\right]\left[\frac{m^*}{2}i\Omega\alpha(\Omega)\right]. \tag{4}$$

Since the units of our spin current is $\hbar/2$, the above expression is a complete analogy to the electric conductivity. Instead of an electric driving force eE, here we have an

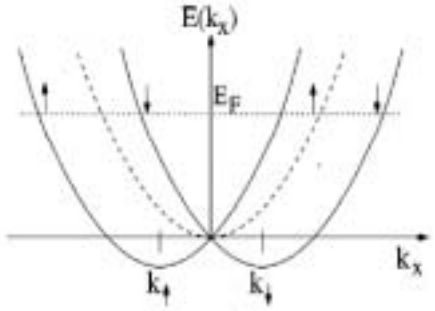

FIG. 1. The dashed curve is the electron energy band without SOI. The SOI splits the energy band into the ↑-spin and the ↓-spin bands, as shown by the solid curves, with corresponding average wave vectors $k_\uparrow$ and $k_\downarrow$.

equivalent driving force $(m^*/2)[d\alpha(t)/dt]$, the Fourier component of which is $(m^*/2)i\Omega\alpha(\Omega)$. Under this driving force we have the classic equation of motion

$$m^*\frac{dv_{\uparrow,\downarrow}}{dt}=\pm\frac{m^*}{2}\frac{d\alpha(t)}{dt}. \tag{5}$$

This force acts in opposite directions on electrons with opposite spin projections. When such a force creates a spin current, it does not induce an electric current.

The above conclusion of spin-current generation can be demonstrated with a rigorous linear response analysis, which will be performed on a 2D electron gas (2DEG). The simple Drude expression (4) will then appear as a general result. Let the 2DEG be in the xy plane with the unit vector $\hat{\nu}$ along the z axis, which is the spin-quantization axis. We will use the equation of motion for the spin-density operator to generalize the 1D expressions (1), (2) for the spin current. For a homogeneous system the spin-current density operators can be expressed in terms of the electron creation operator $c^\dagger_{\vec{k},\gamma}$ and destruction operator $c_{\vec{k},\gamma}$, where γ labels the spin projection onto the z axis. This current is then derived as

$$\mathcal{J}^i_j=J^i_j+J^i_{j,\mathrm{SOI}}, \tag{6}$$

where the superscript $i=x,y,z$ specifies the direction of spin polarization, and the subscript $j=x,y$ refers to the direction of the spin-current flow. The partial current

$$J^i_j=\sum_{\vec{k}}\sum_{\gamma\beta}\frac{\hbar^2k_j}{m^*}c^\dagger_{\vec{k},\gamma}s^i_{\gamma\beta}c_{\vec{k},\beta} \tag{7}$$

is the ordinary kinematic term and

$$J^i_{j,\mathrm{SOI}}=\varepsilon^{ijz}\hbar\alpha n/4 \tag{8}$$

is the contribution of SOI.[7] Here ε^{ijz} denotes the Levy-Civita symbol. The SOI induced current resembles the diamagnetic current of electrons under the action of an external electromagnetic vector potential.

We note that the SOI Hamiltonian can be conveniently written in terms of the kinematic current as

$$H_{\mathrm{SO}}(t)=[m^*\alpha(t)/\hbar](J^x_y-J^y_x). \tag{9}$$

When an ac bias with frequency Ω is applied to the front or the back gate of a 2DEG,[3,4] the Rashba coupling constant contains two terms $\alpha(t)=\alpha_0+\delta\alpha(t)$, where α_0 is constant in time and $\delta\alpha(t)=\delta\alpha e^{i\Omega t}$. We assume that the only effect of the ac bias is to add a time-dependent component to the SOI coupling constant, although in practice it is not simple to avoid the bias effect on the electron density.[4] The SOI Hamiltonian is separated correspondingly into two parts $H_{\mathrm{SO}}(t)=H^0_{\mathrm{SO}}+H'_{\mathrm{SO}}(t)$. The time-independent part H^0_{SO} does not produce a net spin current in the thermodynamically equilibrium state. However, as pointed out in the above analysis on the 1DEG system, the time-dependent $H_{\mathrm{SO}}(t)$ can give rise to a spin current.

We will incorporate H^0_{SO} into our unperturbed Hamiltonian and treat $H'_{\mathrm{SO}}(t)$ within the linear response regime. The so-generated ac spin current $\langle\mathcal{J}^i_j(t)\rangle$ has the form

$$\langle\mathcal{J}^i_j(t)\rangle=\frac{i}{\hbar}\int_{-\infty}^{t}dt'\langle[H'_{\mathrm{SO}}(t'),J^i_j(t)]\rangle+\varepsilon^{ijz}\hbar\,\delta\alpha(t)n/4. \tag{10}$$

In the above equation the first term can be written in the form $\delta\alpha(t)\mathcal{R}^i_j(\Omega)$. For zero temperature and with $\Omega>0$, the response function $\mathcal{R}^i_j(\Omega)$ can be represented as the Fourier transform of the correlator

$$\mathcal{R}^i_j(t)=-i\frac{\hbar^2}{m^*}\sum_{\vec{k}'\alpha'\beta'}k'_j s^i_{\alpha'\beta'}\times\sum_{\vec{k}\alpha\beta}\vec{h}_{\vec{k}}\cdot\vec{s}_{\alpha\beta}\overline{\langle T\{c^\dagger_{\vec{k}',\alpha'}(t)c_{\vec{k}\beta}\}\rangle\langle T\{c_{\vec{k}',\beta'}(t)c^\dagger_{\vec{k}\alpha}\}\rangle}, \tag{11}$$

where $\vec{h}_{\vec{k}}=\vec{k}\times\hat{\nu}$. In the above equation, the bar over the product of two one-particle Green functions means an ensemble average over impurity positions.

We will use the standard perturbation theory[8] to calculate this ensemble average, which is valid when the elastic scattering time τ due to impurities is sufficiently long such that $E_F\tau\gg\hbar$. We will assume that the electron Fermi energy E_F is much larger than both $\hbar\Omega$ and $\hbar\alpha_0 h_{\vec{k}}$. To the first-order approximation, we neglect the weak localization corrections to the correlator (11), since these corrections simply renormalize the spin-diffusion constant.[8] Consequently, the configuration average of the pair product of Green functions is expressed in the so-called ladder series.[9] We found that since $\vec{h}_{\vec{k}}=-\vec{h}_{-\vec{k}}$ many of such ladder diagrams vanish after angular integration in Eq. (11), similar to suppression of ladders in the electric current driven by the vector potential.[9] At the same time, some of nondiagonal on spin indice diagrams do not turn to 0 after the angular integration. Employing the analysis of similar diagrams done in it can be shown that they cancel each other.[8] Hence, the configuration average in Eq. (11) decouples into a product of average Green functions and Eq. (11) becomes

$$\mathcal{R}_j^i(\Omega) = -i\frac{\hbar^2}{m^*}\sum_{l,n}\varepsilon^{lnz}\sum_{\vec{k}} k_j k_n \times \int \frac{d\omega}{2\pi}\mathrm{Tr}[s^l G(\vec{k},\omega) s^i G(\vec{k},\omega+\Omega)], \quad (12)$$

where $G(\vec{k},\omega)$ is the average Green's function which contains fully the effect of H_{SO}^0. This function is represented by the 2×2 matrix

$$G(\vec{k},\omega) = [\omega - E_{\vec{k}}^{\zeta}/\hbar - \alpha_0 \vec{b}_{\vec{k}}\cdot\vec{s} + i\Gamma\,\mathrm{sgn}(\omega)]^{-1}, \quad (13)$$

where $\Gamma = 1/2\tau$, and $E_{\vec{k}}^{\zeta}$ is defined with respect to E_F. Substituting Eq. (13) into Eq. (12), and then into Eq. (10), we obtain the spin current

$$\langle \mathcal{J}_j^i(\Omega)\rangle = \varepsilon^{ijz}\frac{\hbar}{4}\delta\alpha n\frac{\Omega}{\Omega + 2i\Gamma}. \quad (14)$$

It is important to point out that the spin density under the gate area is zero. This is the reason why even in a 2DEG the D'yakonov-Perel spin relaxation[10] does not appear in Eq. (14) for the generated spin current, although this spin current is determined by the response function (12) which involves spin degrees of freedom. Hence, in the homogeneous system with zero spin density, only electron momentum relaxation occurs in the process of spin-current generation by a time-dependent gate.

Unlike the spin current (4) in a 1D system, in a 2DEG the current given by Eq. (14) has no specific direction. To clarify the spatial distribution of the spin flux induced by an ac gate, let us take the chiral component $\mathcal{J}_{\mathrm{chir}}(t)$ of the spin current

$$\mathcal{J}_{\mathrm{chir}}(t) = [\langle \mathcal{J}_y^x(t)\rangle - \langle \mathcal{J}_x^y(t)\rangle]/2. \quad (15)$$

It is easily seen that this chiral projection has the same form as the expression (4) for a 1D system, if n represents the electron density of the 2DEG. In Fig. 2 we illustrate the spin-current distribution for a circular gate which is marked as the gray area. The spin polarization at any point under the gate has two components parallel to the 2DEG. For any direction specified by the unit vector $\vec{N}$, the two spin-polarized fluxes with polarization directions parallel and antiparallel to $\vec{N}$ will oscillate out of phase by the amount of π along the direction perpendicular to $\vec{N}$. Such out of phase oscillation is schematically plotted in Fig. 2. The amplitude of the spin density flow in each of the opposite directions, as marked by the dashed-line arrows, is just $\mathcal{J}_{\mathrm{chir}}(t)$. In the 2DEG outside the gate area, the spin current can be supported only by spin diffusion. Therefore the chiral ac spin polarization is accumulated in the vicinity of the circumference of the gate, and from where diffuses away from the gate area. It can also diffuse under the gate. For small gates such back diffusion can diminish the efficiency of the spin generation. On the other hand, for large gates with the size larger than the spin-diffusion length the diffusion counterflow does not reduce much the total spin current.

The so-generated current amplitude can be easily estimated. With $\delta\alpha = 3\times 10^6$ cm/s,[4] for $\Omega = 2\pi\times 10^9$ s^{-1}, $n = 10^{12}$ cm^{-2}, and $\tau = 1$ ps, from (14) we derive $(2e/\hbar)\times\langle \mathcal{J}_j^i(\Omega)\rangle \simeq 10^{-3}$ Amp/cm. This ac spin current can be detected by various methods. For example, if holes can tunnel into the neighborhood of the gate edge, their recombination with spin-polarized electrons will produce the emission of circular-polarized light.[11]

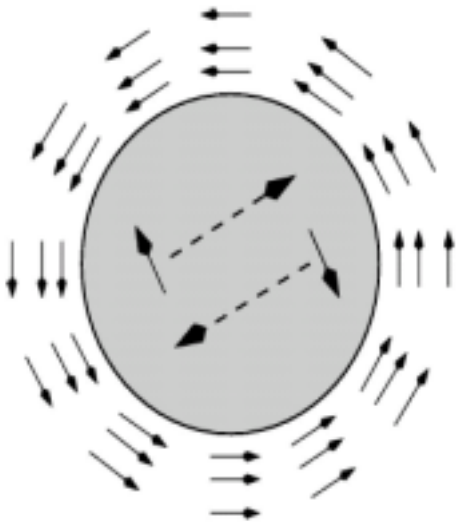

FIG. 2. Distribution of spin currents induced by a time-dependent circular gate which is marked as the gray region. Under the gate, electrons with opposite spins (solid arrows) move in opposite directions indicated by the dashed-line arrows. Arrows outside the gate area show the accumulated spin polarization during a half period of ac gate voltage oscillation.

However, here we will discuss a method of direct electric detection of the dc or the ac spin current. This method is based on a simple fact that the Rashba SOI couples the spin current to the gate voltage. We have shown in our above analysis that due to this coupling, spin current can be induced by a time-dependent gate voltage. In this case the voltage variation plays the role of a source which drives electrons out of thermodynamic equilibrium, and the spin current is the linear response to this perturbation. The reverse process is to create a spin current in a 2DEG by some source, and so inducing a voltage shift in a nearby gate. This is also possible to realize. We thus consider a model where the SOI constant $\alpha(U)$ is a function of the gate voltage $U(t) = U_0 + V(t)$. U_0 is the static equilibrium value in the absence of a spin current, while $V(t)$ is a dynamic variable. The mean value $\langle V\rangle$ of $V(t)$ has to be calculated as a linear response to the perturbation associated with the presence of the spin-polarization flow. The explicit form of this perturbation can be obtained by averaging the Hamiltonian of the system over an electronic state with the given time-dependent spin current.

Let $\langle\cdots\rangle_J$ be such type of average. To the lowest order with respect to SOI, the coupling of the gate voltage to the spin current is thus determined by the average of the Rashba interaction in Eq. (9) with $\alpha = \alpha(U)$. The coupling between the gate voltage $U(t)$ and the spin current $\mathcal{J}_j^i$ is via the kinetic current J_j^i. To derive the coupling Hamiltonian H_{int}, we use Eq. (6) to express J_j^i in terms of $\mathcal{J}_j^i$, and expand

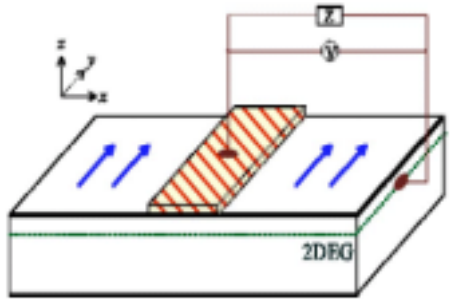

FIG. 3. Schematic illustration of spin current detection. ac spin current flows from the right to the left under the gate with spin polarized as shown by arrows. V denotes the voltmeter and Z is the outer circuit impedance.

$\alpha(U)=\alpha(U_0)+\alpha' V(t)$ for small $V(t)$. The coupling Hamiltonian is then derived from Eq. (9) as

$$H_{\rm int}=\frac{m^*\alpha'}{\hbar}V[\langle\mathcal{J}_y^z\rangle_J-\langle\mathcal{J}_j^z\rangle_J]. \tag{16}$$

The charging of the gate $Q=CV$ is related to the gate capacitance. Hence, Eq. (16) can be expressed in the convenient form $H_{\rm int}=Q\mathcal{E}$, where

$$\mathcal{E}=\frac{m^*\alpha'}{\hbar C}[\langle\mathcal{J}_y^z\rangle_J-\langle\mathcal{J}_j^z\rangle_J] \tag{17}$$

is the effective electromotive force.

To illustrate our proposed method of direct electric detection, let us consider a circuit connected to the gate. The principal scheme of the spin current detection is shown in Fig. 3. In it, an additional back gate can be utilized to tune the electron density (not shown). The circuit is characterized by a frequency-dependent impedance $Z(\Omega)$. The voltage induced on the gate by the electromotive force (17) is then easily obtained as

$$\langle V\rangle=\mathcal{E}\frac{i\Omega CZ(\Omega)}{1+i\Omega CZ(\Omega)}. \tag{18}$$

When the spin-current frequency is in resonance with the circuit eigenmode, the gate voltage becomes very large. In the limit of high impedance (open circuit), $\langle V\rangle=\mathcal{E}$. Using the spin current $(2e/h)\langle\mathcal{J}_j^z(\Omega)\rangle\simeq 10^{-3}$ Amp/cm derived above, and the fact that $\langle\mathcal{J}_j^z\rangle_J=A\langle\mathcal{J}_j^z(\Omega)\rangle$, where A is the area under the gate, let us estimate the electromotive force induced in a probe gate by this spin current generated by a nearby source gate. For the reasonable parameter values $\alpha'=3\times10^7$ cm/Vs,[4] $m^*=0.03\,m_e$, and $C=\kappa\epsilon_0 A/l$ with $\kappa=10$ and $l=10^{-5}$ cm, from Eqs. (14) and (18) we obtain $\mathcal{E}\simeq 10^{-5}$ V.

The generated ac spin current can be rectified with various methods. For example, one can use a shutter gate which is $\pi/2$ phase shifted with respect to the generation gate. The shutter gate can be placed in the neighborhood of the generation gate or between two such gates. The evaluation of the rectifying efficiency of such a setup requires a thorough analysis of spin relaxation and diffusion processes caused by the spin accumulation during the shutter cycle.

We would like to add one relevant piece of information which we became aware of after we completed this paper. The preprint of Governale *et al.* on the quantum-spin pumping in a 1D wire is also based on the idea of creating spin current via a time-dependent gate.[12] However, our results involving dissipative transport in 2DEG and 1DEG cannot be compared directly to those in Ref. 12.

This work was supported by the National Science Council of Taiwan under Grant Nos. 91-2119-M-007-004 (NCTS), 91-2112-M-009-044 (CSC), the Swedish Royal Academy of Science, and the Russian Academy of Sciences and the RFBR Grant No. 03-02-17452. A.G.M. acknowledges the hospitality of NCTS in Hsinchu where this work was initiated.

[1] S. Datta and B. Das, Appl. Phys. Lett. **56**, 665 (1990).
[2] Yu.A. Bychkov and E.I. Rashba, J. Phys. C **17**, 6039 (1984).
[3] J. Nitta *et al.*, Phys. Rev. Lett. **78**, 1335 (1997); G. Engels *et al.* Phys. Rev. B **55**, R1958 (1997).
[4] D. Grundler, Phys. Rev. Lett. **84**, 6074 (2000).
[5] A.G. Mal'shukov, V. Shlyapin, and K.A. Chao, Phys. Rev. B **66**, 081311(R) (2002); J.C. Egues, G. Burkard, and D. Loss, cond-mat/0209682 (unpublished); M. Governale *et al.*, Phys. Rev. B **65**, 140403(R) (2002).
[6] We ignored the bulk Dresselhaus contribution to SOI, which in narrow gap heterostructures is believed to be negligible in comparison with the Rashba effect. See discussion in Ref. 4.
[7] U. Zulicke and C. Schroll, Phys. Rev. Lett. **88**, 029701 (2002).
[8] A.G. Mal'shukov, K.A. Chao, and M. Willander, Phys. Rev. Lett. **76**, 3794 (1996); Phys. Scr. **T66**, 138 (1996).
[9] B. L. Altshuler and A. G. Aronov, in *Electron-Electron Interactions in Disordered Systems*, edited by A. L. Efros and M. Pollak (North-Holland, Amsterdam, 1985).
[10] M.I. D'yakonov and V.I. Perel, Fiz. Tverd. Tela **13**, 3581 (1971) [Sov. Phys. Solid State **13**, 3023 (1972)]; Zh. Eksp. Teor. Fiz. **60**, 1954 (1971) [Sov. Phys. JETP **33**, 1053 (1971)].
[11] R. Fiederling *et al.*, Nature (London) **402**, 787 (1999); Y. Ohno *et al.*, *ibid.* **402**, 790 (1999).
[12] M. Governale, F. Taddei, and R. Fazio, Phys. Rev. B **68**, 155324 (2003).

Appendix C:

PHYSICAL REVIEW B 70, 085315 (2004)

Finger-gate array quantum pumps: Pumping characteristics and mechanisms

S. W. Chung,[1] C. S. Tang,[2] C. S. Chu,[3] and C. Y. Chang[1]
[1]*Department of Electronics, National Chiao-Tung University, Hsinchu 30010, Taiwan*
[2]*Physics Division, National Center for Theoretical Sciences, P.O. Box 2-131, Hsinchu 30013, Taiwan*
[3]*Department of Electrophysics, National Chiao-Tung University, Hsinchu 30010, Taiwan*
(Received 7 June 2003; revised manuscript received 19 March 2004; published 27 August 2004)

We study the pumping effects, in both the adiabatic and nonadiabatic regimes, of a pair of *finite* finger-gate array (FGA) on a narrow channel. Connection between the pumping characteristics and associated mechanisms is established. The pumping potential is generated by ac biasing the FGA pair. For a single pair ($N=1$) of finger gates (FG's), the pumping mechanism is due to the coherent inelastic scattering of the traversing electron to its subband threshold. For a pair of FGA with pair number $N>2$, the dominant pumping mechanism becomes that of the time-dependent Bragg reflection. The contribution of the time-dependent Bragg reflection to the pumping is enabled by breaking the symmetry in the electron transmission when the pumping potential is of a predominant propagating type. This propagating wave condition can be achieved both by an appropriate choice of the FGA pair configuration and by the monitoring of a phase difference ϕ between the ac biases in the FGA pair. The robustness of such a pumping mechanism is demonstrated by considering a FGA pair with only pair number $N=4$.

DOI: 10.1103/PhysRevB.70.085315 PACS number(s): 72.10.−d, 72.30.+q, 72.90.+y

I. INTRODUCTION

Quantum charge pumping (QCP) has become an active field in recent years.[1–21] This is concerned with the generation of net transport of charges across an unbiased mesoscopic structure by cyclic deformation of two structure parameters. Original proposal of QCP, in the adiabatic regime, was due to Thouless[1,2] and Niu.[2] They considered the current generated by a slowly varying traveling wave in an isolated one-dimensional system. The number of electrons transported per period was found to be quantized if the Fermi energy lies in a gap of the spectrum of the instantaneous Hamiltonian. Aiming at this quantized pumped charge nature of the adiabatic pumping, Niu proposed various one-dimensional periodic potentials for the adiabatic quantum pumping (AQP),[2] and pointed out the importance of the quantized charge pumping in utilizing it for a direct-current standard.[2]

Another way to achieve the AQP was suggested by Hekking and Nazarov,[3] who studied the role of inelastic scattering in the quantum pumping of a double-oscillating barrier in a one-dimensional system. Intended to stay in the adiabatic regime, they invoked a semiclassical approximation and had assumed that the Fermi energy $\varepsilon_F \gg \hbar\Omega$, where Ω is the pumping frequency. This semiclassical treatment of the inelastic scattering is known to be inappropriate for the regime when either the initial or the final states are in the vicinity of the energy band edge. Such a regime, however, is our major focus in this work. It is because the coherent inelastic scattering becomes resonant when the traversing electron can make transitions to its subband threshold by emitting $m\hbar\Omega$.[22,23] Depending on the system configuration, this and another resonant inelastic scatterings will be shown to dominate the pumping characteristics.[10]

A recent experimental confirmation of AQP has been reported by Switkes *et al.*[4] Two metal gates that defined the shape of an open quantum dot were ac biased[24] with voltages of the same frequency but differed by a tunable phase difference.[5] DC response across the source and drain electrodes is the signature of the AQP. This has prompted further intensive studies on AQP in quantum dots,[6–8] double-barrier quantum wells,[9] pumped voltage,[12] noiseless AQP,[13] heat current,[14] incoherent processes,[15,16] quantum rings,[19,20] and interacting wires.[21]

An alternate experimental effort in generating AQP involves surface acoustic wave (SAW).[25–29] Generated by an interdigitated SAW transducer located deep on an end-region of a narrow channel, the SAW propagates to the other end-region of the narrow channel while inducing a wave of electrostatic potential inside the channel. Electrons trapped in the potential minima are thus transported along the narrow channel. Both Mott-Hubbard electron-electron repulsion in each such trap and the adiabaticity in the transport are needed to give rise to quantization in the pumped current.[26] As such, the channel has to be operated in the pinch-off regime.[27]

In this work, we propose to study yet another experimental configuration for QCP in a narrow channel. The proposed configuration consists of a pair of *finite* finger-gate array (FGA), with the number N of FG's in each FGA being kept to a small number. In contrast to the SAW configuration, the FGA pair sits on top of the narrow channel, rather than locating at a distance far away from it and the most significant QCP occurs in regimes other than the pinch-off regime. The FG's orient transversely and line up longitudinally with respect to the narrow constriction. As is shown in Fig. 1, pumping potential can be generated by ac biasing the FGA pairs with the same frequency but maintaining a phase difference ϕ between them. Since the wave of electrostatic potential induced in the narrow channel is directly from the FG's, rather than via the SAW, our proposed structure has the obvious advantage that the working frequency is not restricted to the frequency of the SAW, $\omega_S = 2\pi v_S/d$. Here v_S is the phase velocity of the SAW, and d is the pitch in the FGA. Furthermore, when the working frequency is different from

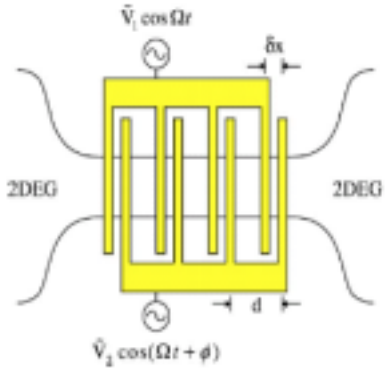

FIG. 1. (Color online) Top view of the proposed system structure for the case of pair number $N=4$. A FGA pair is located on top of a narrow channel. $\tilde{V}_i$ denotes the amplitude of the potential energy, and ϕ is the phase difference.

ω_S, the contribution from SAW to the pumped current will be negligible.

Below we shall show how the ac biased FGA pair plays a subtle role in the generation of QCP. In Sec. II, we present our theoretical model for the FGA pair calculation of the pumped current generated by the FGA pair configuration. In Sec. III, we present the pumping characteristics and demonstrate that resonant coherent inelastic scatterings are the underlying pumping mechanisms. Finally, in Sec. IV, we present our discussion and summary.

II. FGA PAIR MODEL

The potential $V(x,t)$ in a narrow constriction induced by a FGA pair is represented by

$$V(x,t)=\sum_{i=1}^{N} V_{1i}(x)\cos(\Omega t)+V_{2i}(x)\cos(\Omega t+\phi), \quad (1)$$

where N is the number of FG's per FGA. We assume that the ac biased FGA pair are localized, respectively, at positions x_i and $x_i+\delta x_i$, namely, that $V_{1i}(x)=V_1\delta(x-x_i)$ and $V_{2i}(x)=V_2\delta(x-x_i-\delta x)$ with a relative phase difference ϕ. These FG's are evenly spaced, with a pitch d, and are located at $x_i=(i-1)d$ for one FGA and $x_i+\delta x$ for the other. The relative shift between the FGA pair is $\delta x=\alpha d$, where the fractional shift $0<\alpha<1$. In the following, we consider the case of the same modulation amplitude $V_1=V_2=V_0$. Depending on the choice of the values for ϕ and α, $V(x,t)$ will either be predominantly of a propagating or a standing wave type. A sensible choice can be made from considering the lowest order Fourier component of $V(x,t)$, given by

$$V_1=\frac{2V_0}{d}\{\cos Kx\cos\Omega t+\cos[K(x-\delta x)]\cos(\Omega t+\phi)\}, \quad (2)$$

where $K=2\pi/d$. For our purposes in this work, an optimal choice is $\phi=\pi/2$ and $\alpha=1/4$, in which $V(x,t)$ is a predominant left-going wave.

The Hamiltonian of the system is $H=H_y+H_x(t)$, in which $H_y=-\partial^2/\partial y^2+\omega_0^2y^2$ contains a transverse confinement, leading to subband energies $\epsilon_n=(2n+1)\omega_y$. The time-dependent part of the Hamiltonian $H_x(t)$ is of the dimensionless form $H_x(t)=-\partial^2/\partial x^2+V(x,t)$. Here appropriate units have been used such that all physical quantities presented are in dimensionless form.[24]

In the QCP regime, the chemical potential μ is the same in all reservoirs. Thus the pumped current, at zero temperature, can be expressed as[10]

$$I=-\frac{2e}{h}\int_0^{\mu} dE\,[T_{-}(E)-T_{-}(E)]. \quad (3)$$

Here the total current transmission coefficients include the contributions by electrons with incident energy E in incident subband n, which may absorb or emit $m\Omega$ to energy $E_m=E+m\Omega$ by the FG pumping potentials, given by

$$T_{-(\leftarrow)}(E)=\sum_{n=0}^{N_S-1}\sum_{m=-\infty}^{\infty} T_{n\to(\leftarrow)}(E_m,E), \quad (4)$$

where N_S stands for the number of occupied subbands. The summations are over all the propagating components of the transmitted electrons, and includes both the subband index n and the sideband index m. The subscripted arrow in the total current transmission coefficient indicates the incident direction. These coefficients are calculated numerically by a time-dependent scattering-matrix method.[10,30,31]

III. NUMERICAL RESULTS

In this section we present the numerical results for the pumping characteristics of either a single FG pair ($N=1$) or a *finite* FGA pair ($N>2$). In these two cases the pumping characteristics are due to different resonant inelastic scattering processes. For definiteness, the parameter values in our numerical results are taken from the FaAs-$Al_xGa_{1-x}As$ based heterostructure. The values that we choose for our configuration parameters are $\omega_y=0.007$, subband level spacing $\Delta\varepsilon=2\omega_y(\simeq 0.13$ meV), $d=40$ ($\simeq 0.32$ μm), and $V0=0.04$ ($\simeq 28.7$ meV Å). From the value of V_0, and the assumed FG width ~ 0.05 μm, the amplitude of the potential induced by a FG is ~ 0.057 mV.

A. Single FG pair case

In this subsection we investigate the pumping characteristics for the case of a single FG pair. Figure 2 presents the dependence of the total current transmission coefficients on the incident electron energy μ. We replace the chemical potential μ by

$$X_\mu=\frac{\mu}{\Delta\varepsilon}+\frac{1}{2}, \quad (5)$$

which integral value corresponds to the number of propagating subbands N_S in the narrow channel. The pumping frequency is higher in Fig. 2(a), with $\Omega=0.6\Delta\varepsilon(\Omega/2\pi\simeq 18$ GHz), than that in Fig. 2(b), where $\Omega=0.1\Delta\varepsilon(\Omega/2\pi\simeq 3$ GHz). We select the phase shift $\phi=\pi/2$ and $\alpha=1/4$.

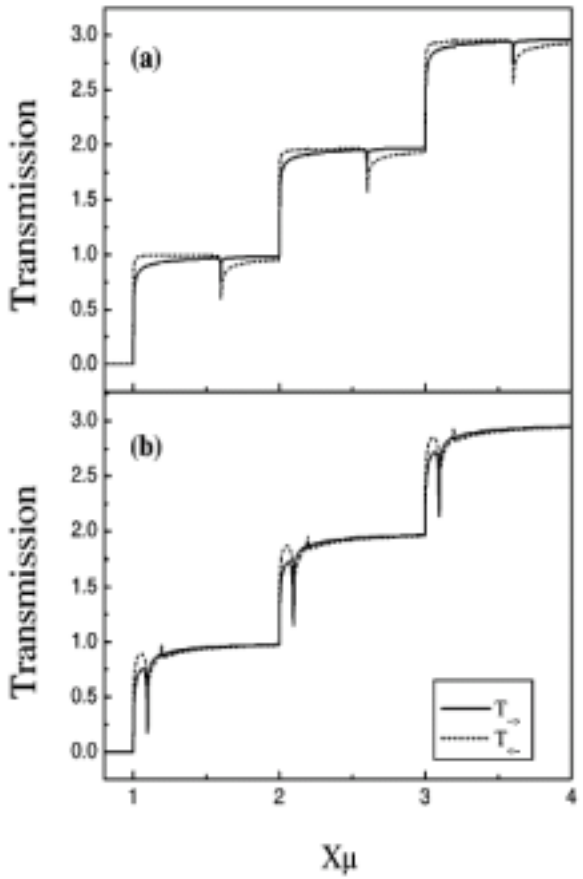

FIG. 2. Total current transmission coefficient versus X_μ for a pair of FG, (a) $\Omega=0.6\Delta\varepsilon$ and (b) $\Omega=0.1\Delta\varepsilon$. The transmission of the right-going (left-going) electrons are represented by the solid (dotted) curve. The subband level spacing is $\Delta\varepsilon$. Parameters $\alpha=1/4$ and $\phi=\pi/2$ are chosen to meet the optimal condition.

At integral values of X_μ, the total current transmission coefficients $T_{\rightarrow(\leftarrow)}(X_\mu)$ exhibit abrupt changes. This is due to the changes in the number of propagating subbands in the narrow channel. Between integral X_μ values, $T_{\rightarrow(\leftarrow)}$ both show dip structures. The dip structures are located at $X_{\text{dip}}=\mathcal{N}_S+0.6$ in Fig. 2(a), and at $X_{\text{dip}}=\mathcal{N}_S+0.1$ in Fig. 2(b). These dip structure locations are the same for both $T_{\rightarrow}$ and $T_{\leftarrow}$, and are resonant structures associated with inelastic scattering that causes an electron to jump into a quasibound state (QBS) just beneath a subband bottom.[22] The peak structures in $T_{\leftarrow}$ of Fig. 2(b), and at $X_\mu=\mathcal{N}_S+0.2$, are 2Ω resonant structures.

In Fig. 2, we can see that $T_{\leftarrow}(X_\mu)$ does not equal to $T_{\rightarrow}(X_\mu)$, this allows the occurrence of the pumped current. Moreover, between integral X_μ values, $T_{\leftarrow}>T_{\rightarrow}$ on the left region of a dip structure, while $T_{\leftarrow}<T_{\rightarrow}$ on the right region of the dip structure. This has an important bearing on the dependence of the pumped current on μ, as is shown in Fig. 3. The pumped current rises, and drops, on the left, and right, region of a X_{dip}, respectively, in accordance with the relative changes in $T_{\rightarrow}$ and $T_{\leftarrow}$ about the same X_{dip}. Hence the peaks of the pumped current depend on the pumping frequency, at

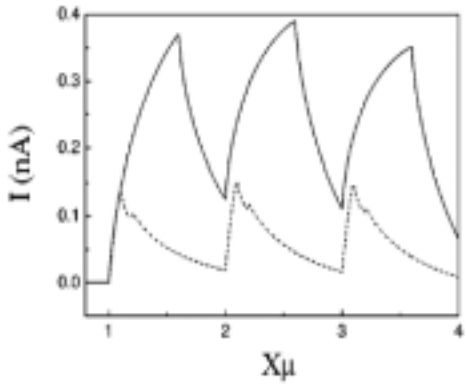

FIG. 3. The pumped currents versus X_μ with the same parameters used in Fig. 2. The solid and dashed curves correspond, respectively, to $\Omega=0.6\Delta\varepsilon$ and $\Omega=0.1\Delta\varepsilon$.

$$X_\mu^{(\text{peak})}=\mathcal{N}_S+\frac{\Omega}{\Delta\varepsilon}, \tag{6}$$

reassuring us that the pumping is dominated by the aforementioned resonant inelastic process.

Besides the trend that the pumped current in Fig. 3 drops with the pumping frequency, we would like to remark on a more interesting result: that both the adiabatic and nonadiabatic behaviors can be found in the same curve. Since the adiabatic condition is given by $\mu \gg \Omega$, the curve for $\Omega=0.1\Delta\varepsilon$ in the regions $\mathcal{N}_S+\Omega/\Delta\varepsilon<X_\mu\leqslant\mathcal{N}_S+1$ corresponds to the adiabatic regimes, while the other X_μ regions are nonadiabatic regimes. This is checked also with our other calculation, which is not shown here, using the Brouwer expression.[5] For the higher pumping frequency, $\Omega=0.6\Delta\varepsilon$, the adiabatic condition is not satisfied in the entire X_μ region, even though the pumping characteristics resemble that of the adiabatic one in the regions $\mathcal{N}_S+\Omega/\Delta\varepsilon<X_\mu\leqslant\mathcal{N}_S+1$.

B. Finite FGA case

In this subsection we present the numerical results for the pumping characteristics of a *finite* FGA pair. QCP for two prominent modes of tuning the system are considered. These are (i) tuning of the electron density by the *back-gate* technique, and (ii) tuning of the channel width by *split-gate* technique.

1. Tuning back-gate

We present the numerical results for the pumping characteristics of a FGA pair with $N=4$ that is realized by the *back-gate technique*. The dependence of the total current transmission coefficients on X_μ is shown in Fig. 4, in which the pumping frequencies are (a) $\Omega=0.6\Delta\varepsilon$ and (b) $\Omega=0.1\Delta\varepsilon$. The choice of the parameters d, ϕ, and α is the same as in the previous subsection, but the latter two parameters give rise here to an equivalent left-going wave in the pumping potential $V(x,t)$.

The curves in Fig. 4 show additional structures, other than the dip structures that has been discussed in the last subsection. These additional structures are valley structures that occur at different X_μ values for $T_{\rightarrow}(X_\mu)$ and $T_{\leftarrow}$. In a region

between two integral values of X_μ, the valley structure of $T_{-+}(X_\mu)$ occurs at a lower X_μ. This shows clearly the breaking of the transmission symmetry by the pumping potential. Furthermore, the valleys are separated by $\Delta X_\mu = \Omega/\Delta\varepsilon$. This can be understood from resonant coupling conditions $\varepsilon_k = \varepsilon_{k-K} - \Omega$ and $\varepsilon_{k+K} = \varepsilon_k - \Omega$ for, respectively, the right-going and the left-going k. From these conditions, the valley locations are at

$$k_\pm^2 = \left[\frac{K}{2}\left(1 \mp \frac{\Omega}{K^2}\right)\right]^2, \tag{7}$$

where the upper sign is for positive, or right-going, k. These locations, expressed in terms of X_μ, are given by

$$X_\mu = N_S + \frac{k_\pm^2}{\Delta\varepsilon}, \tag{8}$$

and are at $X_\mu = 1.19$, 1.79, 2.19, 2.79, 3.19, and 3.79 for the case of Fig. 4(a), and $X_\mu = 1.39$, 1.49, 2.39, 2.49, 3.39, and 3.49 for the case of Fig. 4(b). The matching between these numbers and our numerical results in Fig. 4 is remarkable. In addition, energy gaps open up at these $k_\pm^2$ locations, causing the drop in the transmission and the formation of the valley structures.[10] All these results reassure us that the time-dependent Bragg's reflection is the dominant resonant inelastic scattering in our FGA pair structure.

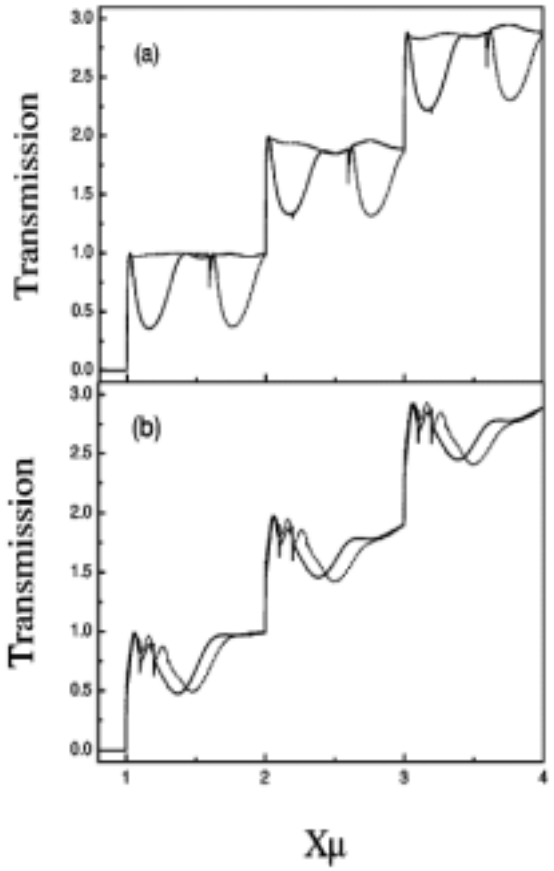

FIG. 4. Total current transmission coefficient versus X_μ for $N = 4$; (a) $\Omega = 0.6\Delta\varepsilon$ and (b) $\Omega = 0.1\Delta\varepsilon$. The transmission of the right-going (left-going) electrons are represented by the solid (dotted) curve. The parameters $\alpha = 1/4$ and $\phi = \pi/2$.

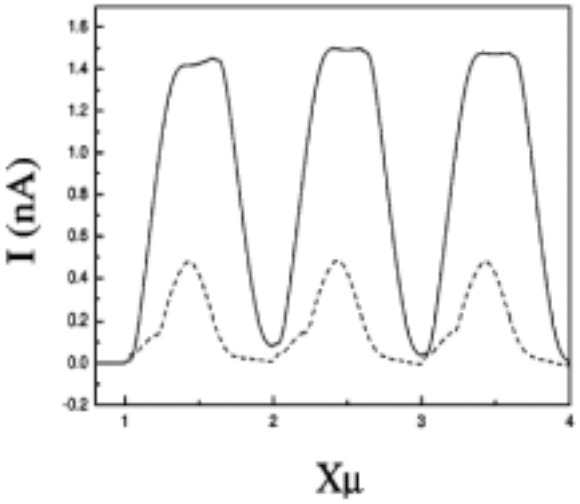

FIG. 5. Pumped current versus X_μ. The choices of parameters are the same as in Fig. 4. The solid and dashed curves correspond, respectively, to $\Omega = 0.6\Delta\varepsilon$ and $\Omega = 0.1\Delta\varepsilon$.

On the other hand, the adiabatic condition is here given by $\varepsilon_{gap} \gg \Omega$, where ε_{gap} is the *effective* energy gap of the *instantaneous* Hamiltonian.[2] Since ε_{gap} is given by the widths of the valley structures, therefore contributions of the valleys to the pumped current is nonadiabatic in Fig. 4(a), because the valleys are well separated, and adiabatic in Fig. 4(b), because the valleys overlap.

In Fig. 5, we present the X_μ dependence of the pumped current for the cases in Fig. 4. The pumped current peaks at X_μ that lies in the middle between a valley in $T_{-+}(X_\mu)$ and the corresponding valley in $T_{+-}(X_\mu)$. The locations are around

$$X_\mu = N_S + \frac{K^2}{4\Delta\varepsilon}\left(1 + \frac{\Omega^2}{K^4}\right), \tag{9}$$

which depend on both the pitch d and the pumping frequency Ω. The peaks have flat tops for the solid curve, when $\Omega = 0.6\Delta\varepsilon$. Comparing with the total current transmission curves in Fig. 4(a), we see that the flat-topped peak profile is associated with the complete separation between the valleys in T_{-+} and T_{+-}. This is in the nonadiabatic regime. In contrast, for the case when the valleys overlap, such as in Fig. 4(b), the pumped current peaks no longer carry a flat-top profile, as is shown by the dashed curve in Fig. 5. This is in the adiabatic regime. Meanwhile, their peak values are lowered. It is because cancellation sets in when the valleys overlap. We note that the pumped currents are of order nA.

The robustness of the time-dependent Bragg reflection, on the other hand, is demonstrated most convincingly by the number of charge pumped per cycle at the maximum I_{3Max} of the pumped current. In the dashed curve of Fig. 5, the pumped charge per cycle per spin state $Q_P = (2\pi/\Omega) I_{3Max}/2e = 0.495$, where $I_{3Max} = 0.48$ nA and $\Omega = 0.1\Delta\varepsilon = 3.03$ GHz. To get a unity, or quantized, charge pumped per cycle per spin state, one can fix the pumping frequency $\Omega = 0.1\Delta\varepsilon$, $N = 4$, $\phi = \pi/2$, and $d = 40$, then tune the

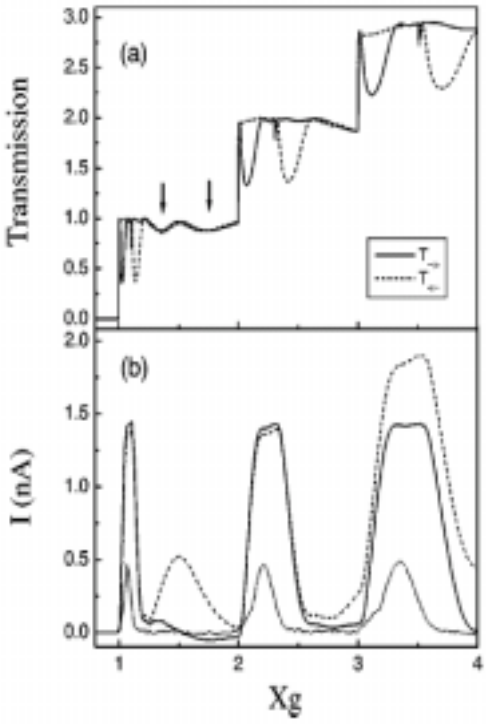

FIG. 6. The dependence on subband level spacing $\Delta\varepsilon$ of (a) the total current transmission coefficient, and (b) the pumped current. The abscissa is depicted by Eq. (10) where $\mu=0.049$ and $N=4$. Pumping frequency $\Omega=0.0084$ in all curves except for the dotted curve in (b), where $\Omega=0.0014$. Parameters $\phi=\pi/2$ and $\alpha=1/4$ for all curves except for the dashed curve in (b), where $\alpha=1/5$. In (a), the solid (dashed) curve is for $T_{-}(X_g)[T_{-}(X_g)]$, and contributions from the second Fourier component of $V(x,t)$ are indicated by arrows.

other pumping parameters $V_0=0.09$ and $\alpha=0.15$ to obtain $Q_P=0.992$ at $X_\mu=3.465$ (not shown here). In this frequency regime, the pumping would be expected to be adiabatic, according to Thouless[1] and Niu[2] when $\varepsilon_{gap}\gg\Omega$. However, in our case here, the energy gap is at best only partially opened, as we can see from the nonzero transmission in Fig. 4(b), because we have only $N=4$ FG pairs. Thus our result shows that the condition of occurrence of the AQP is less stringent than we would have expected originally.[2] In other words, the pumping effect of our FGA configuration is robust.

It is also worth pointing out that the pumped currents are positive in Fig. 5, showing that the net number flux of the pumped electrons is from right to left. This is consistent with the propagation direction of the electrostatic wave in $V(x,t)$.[10]

2. Tuning split-gate

Thus far, we have explored the dependence of the FGA pair's QCP characteristics on X_μ by the use of the *back-gate technique*. Another way of tuning the QCP characteristics is via the modulation of the channel width (or subband level spacing $\Delta\varepsilon$). This can be realized experimentally by the use of the so-called *split-gate technique*. Hence we present, in Fig. 6, the transverse confinement dependence of both the total current transmission coefficients and the pumped current. The transverse confinement is depicted by

$$X_g=\frac{\mu}{\Delta\varepsilon}+\frac{1}{2}, \tag{10}$$

which is linearly related to the effective channel width, and that its integral value corresponds to the number of propagating subbands in the channel. In this mode of tuning the QCP characteristics, μ is kept fixed.

In Fig. 6(a), except for μ, which is fixed at 0.049, and ω_1, which varies with X_g, other parameters such as $\Omega=0.0084$, $\phi=\pi/2$, and $\alpha=1/4$ are the same as in Fig. 4(a). The solid (dashed) curve is for T_{-+} (T_{--}). Both the QBS and the time-dependent Bragg reflection features are found. The expected locations of the QBS, given by the expression

$$X_g=\frac{1}{2}+\left(n+\frac{1}{2}\right)\frac{\mu}{\mu-\Omega}, \tag{11}$$

are at 1.1, 2.3, and 3.5, and they match the QBS locations in Fig. 6(a) perfectly. Here n is the subband index. The expected locations of the valleys, associated with the time-dependent Bragg reflection, are given by the expression

$$X_g=\frac{1}{2}+\left(n+\frac{1}{2}\right)\frac{\mu}{\mu-k_n^2}, \tag{12}$$

thus they should be at $X_g=1.03,2.1,3.14$ for $T_{-+}(X_g)$, and at $X_g=1.15,2.4,3.73$ for $T_{--}(X_g)$. Again, they match the valley locations in Fig. 6(a) remarkably.

Besides, there are in Fig. 6(a) two additional valley structures, indicated by arrows, at which $T_{-+}(X_g)$ and $T_{--}(X_g)$ fall one on top of the other. These structures do not contribute to the pumped current, and they are due to the time-dependent Bragg reflection from the second order Fourier component of $V(x,t)$. The second Fourier component of $V(x,t)$ is in the form of a standing wave, given by $\cos(2Kx)[\cos\Omega t+\sin\Omega t]$. That both of the additional valleys all appear in $T_{-+}(X_g)$ and $T_{--}(X_g)$ can be understood from the fact that more resonant coupling conditions come into play for the case of standing wave. The resonant coupling conditions are $\varepsilon_k=\varepsilon_{k\pm2K}\pm\Omega$, and $\varepsilon_k=\varepsilon_{k\pm2K}\mp\Omega$. As such, the valley locations are given by the expression

$$X_g=\frac{1}{2}\left[1+\frac{\mu}{\mu-\epsilon_n}\right] \tag{13}$$

for $n=0$, and for $\epsilon_n=[K(1\mp\Omega/(2K)^2)]^2$. Accordingly, these $2K$ time-dependent Bragg reflection valley locations are expected to be at 1.36 and 1.73, which coincide with the two additional valleys in Fig. 6(a), and are indicated by arrows. We note, in passing, that contributions from higher Fourier components diminish, as is seen by comparing the valleys from the first and the second Fourier components of $V(x,t)$.

The X_g dependence of the pumped current for the case in Fig. 6(a) is represented by the solid curve in Fig. 6(b). The peaks have flat tops because the valleys in the corresponding $T_{-+}(X_g)$, $T_{--}(X_g)$ are well separated. The pumped current for $\Omega=0.0014$, the same frequency as in the case of Fig. 4(b), is depicted by the dotted curve in Fig. 6(b). The peaks are not flat-topped and the magnitudes are much smaller because the

transmission valleys overlap. For comparison, we also present the case when parameter values differ slightly from that of the optimal choice. As is shown by the dashed curve in Fig. 6(b), where all parameters are the same as for the solid curve except that α is changed from 1/4 to 1/5, the basic pumped current peaks in the solid curve remain intact. This demonstrates the robustness of the QCP against the deviation in values of the configuration parameters from the optimal choice.

Interestingly, there are two additional features in the dashed curve of Fig. 6(b): namely, an additional pumped current peak at $X_g=1.5$, and an increase in the peak value for the pumped current near $X_g=3.5$. That both of these features are found to arise from the second Fourier component of $V(x,t)$ is supported by the outcome of our analysis performed upon the Fourier component of $V(x,t)$. This method of analysis has thus far been successful in providing us insights on the pumping characteristics presented in this work. The m-th Fourier component of $V(x,t)$, apart from a constant factor, is given by the form

$$V_m = \{[\cos(m\pi\alpha) - \sin(m\pi\alpha)]\cos[mKx' - \Omega t - \pi/4] + [\cos(m\pi\alpha) + \sin(m\pi\alpha)]\cos[mKx' + \Omega t + \pi/4]\}, \quad (14)$$

where $x'=x-\delta x/2$. $\mathcal{V}_m$ consists, in general, of waves propagating in both left and right directions. But when $\alpha=1/4$, as we have discussed before, $\mathcal{V}_1$ becomes a pure left-going wave and $\mathcal{V}_2$ becomes a pure standing wave. The case of $\alpha=1/5$, however, have both $\mathcal{V}_1$ and $\mathcal{V}_2$ consisting of waves in opposite propagation directions. Therefore, in contrast with the $\alpha=1/4$ result, additional contributions from the $2K$ Bragg reflection are expected for the case $\alpha=1/5$. This additional contribution should peak at the mid-point between two transmission valleys for the $2K$ Bragg reflections, and the expression for X_g is given by

$$X_g = \frac{1}{2} + \left(n + \frac{1}{2}\right)\frac{\mu}{\mu - \epsilon_M}, \quad (15)$$

where $\epsilon_M=K^2+(\Omega/2K)^2$. For the case of the dashed curve in Fig. 6(b), the values of X_g = 1.54 and 3.6 are shown to match the locations of the additional features nicely. Finally, we can extract information of the sensitivity of the pumped current characteristics to α by looking at the coefficients of the left-going and right-going waves in $\mathcal{V}_m$. For $\alpha=1/5$, the coefficients of $\mathcal{V}_1$ for, respectively, the right-going and the left-going waves are 0.22 and 1.4. This shows that $\mathcal{V}_1$ is still dominated by the left-going wave and thus explains the tiny modifications to the pumped current peaks at $X_g=1.1$, and 2.3. But for $\mathcal{V}_2$, the coefficients for, respectively, the right-going and the left-going waves are −0.95 and 1.57. This shows that $\mathcal{V}_2$ deviates quite significantly from that of a standing wave, and so explains that the additional peaks from the $2K$ Bragg reflections are quite large.

IV. DISCUSSION AND SUMMARY

It is interesting to note in passing that our proposal of the FGA pair configuration is different, in three aspects, from the voltage lead pattern proposed earlier by Niu.[2] First of all, the pumping mechanisms to which the configurations are catering to are different. It is the mechanism of translating the Wannier functions in a given Bloch band in Ref. 2, while it is the mechanism of the time-dependent Bragg reflection in this work. The former mechanism is adiabatic by nature but the latter mechanism is shown, in this work, to hold in both the adiabatic and non-adiabatic regimes.

Second, the configurations are different in the number of sets of voltage leads invoked. A third set of voltage leads was instituted by Niu to fix the Fermi energy at the middle of the *instantaneous energy gap* in order to maintain the adiabaticity of the pumping. Since our interest here is on the general pumping characteristics, including, in particular, their dependence on the Fermi energy, it suffices us to consider a simpler configuration—the FGA pair configuration. Third, the number of voltage lead expected, and needed, in a voltage lead set is different. Our results demonstrate the resonant nature of the time-dependent Bragg reflection, and that the pumping characteristic is robust—requiring only a FGA pair with small N. Hence the FGA pair configuration proposed in this work should be more accessible experimentally.

In conclusion, we have proposed a finger-gate array pair configuration for the generation of quantum charge pumping. Detail pumping characteristics have been analyzed, the robustness of the time-dependent Bragg reflection in QCP has been demonstrated, and the pumping mechanism is understood.

ACKNOWLEDGMENT

This work was funded by the National Science Council of Taiwan under Grant Nos. NSC92-2112-M-009-035, NSC92-2120-M-009-010 (CSC), and NSC91-2119-M-007-004 (NCTS).

[1] D. J. Thouless, Phys. Rev. B **27**, 6083 (1983).
[2] Q. Niu, Phys. Rev. Lett. **64**, 1812 (1990).
[3] F. Hekking and Yu. V. Nazarov, Phys. Rev. B **44**, 9110 (1991).
[4] M. Switkes, C. M. Marcus, K. Campman, and A. C. Gossard, Science **283**, 1905 (1999).
[5] P. W. Brouwer, Phys. Rev. B **58**, R10135 (1998).
[6] I. L. Aleiner and A. V. Andreev, Phys. Rev. Lett. **81**, 1286 (1998).
[7] F. Zhou, B. Spivak, and B. Altshuler, Phys. Rev. Lett. **82**, 608 (1999).
[8] O. Entin-Wohlman and A. Aharony, Phys. Rev. B **66**, 035329 (2002).
[9] Y. Wei, J. Wang, and H. Guo, Phys. Rev. B **62**, 9947 (2000).
[10] C. S. Tang and C. S. Chu, Solid State Commun. **120**, 353 (2001).

[11] S. Zhu and Z. D. Wang, Phys. Rev. B **65**, 155313 (2002).
[12] M. L. Polianski and P. W. Brouwer, Phys. Rev. B **64**, 075304 (2001).
[13] J. E. Avron, A. Elgart, G. M. Graf, and L. Sadun, Phys. Rev. Lett. **87**, 236601 (2001).
[14] B. Wang and J. Wang, Phys. Rev. B **66**, 125310 (2002).
[15] M. Moskalets and M. Büttiker, Phys. Rev. B **64**, 201305(R) (2001).
[16] M. Moskalets and M. Büttiker, Phys. Rev. B **66**, 035306 (2002).
[17] S. W. Kim, Phys. Rev. B **68**, 085312 (2003); S. W. Kim, Phys. Rev. B **66**, 235304 (2002).
[18] M. Moskalets and M. Büttiker, Phys. Rev. B **68**, 075303 (2003).
[19] M. Moskalets and M. Büttiker, Phys. Rev. B **68**, 161311 (2003).
[20] D. Cohen, Phys. Rev. B **68**, 201303(R) (2003).
[21] P. Sharma and C. Chamon, Phys. Rev. B **68**, 035321 (2003).
[22] The fact that a coherent inelastic scattering becomes resonant when the traversing electron can make transitions to its band edge by emitting $n\hbar\Omega$ was studied by P. F. Bagwell and R. K. Lake in Phys. Rev. B **46**, 15329 (1992), where they considered the transmission through a single oscillating barrier.
[23] D. F. Martinez and L. E. Reichl, Phys. Rev. B **64**, 245315 (2001).
[24] C. S. Tang, Y. H. Tan, and C. S. Chu, Phys. Rev. B **67**, 205324 (2003).
[25] J. M. Shilton, V. I. Talyanskii, M. Pepper, D. A. Ritchie, J. E. F. Frost, C. J. B. Ford, C. G. Smith, and G. A. C. Jones, J. Phys.: Condens. Matter **8**, L531 (1996); J. M. Shilton, D. R. Mace, V. I. Talyanskii, Yu. Galperin, M. Y. Simmons, M. Pepper, and D. A. Ritchie, J. Phys.: Condens. Matter **8**, L337 (1996).
[26] V. I. Talyanskii, J. M. Shilton, M. Pepper, C. G. Smith, C. J. B. Ford, E. H. Linfield, D. A. Ritchie, and G. A. C. Jones, Phys. Rev. B **56**, 15180 (1997).
[27] Y. Levinson, O. Entin-Wohlman, and P. Wölfle, Phys. Rev. Lett. **85**, 634 (2000).
[28] O. Entin-Wohlman, Y. Levinson, and P. Wölfle, Phys. Rev. B **64**, 195308 (2001).
[29] A. Aharony and O. Entin-Wohlman, Phys. Rev. B **65**, 241401(R) (2002).
[30] A time-dependent transfer matrix method was discussed by M. Wagner, Phys. Rev. A **51**, 798 (1995); Phys. Rev. B **49**, 16544 (1994); M. Henseler, T. Dittrich, and K. Richter, Phys. Rev. E **64**, 046218 (2001).
[31] A detail presentation of a time-dependent scattering matrix method was given by C. S. Tang and C. S. Chu in Physica B **292**, 127 (2000).

Appendix D:

DC Spin Current Generation in a Rashba-type Quantum Channel

L. Y. Wang,[1] C. S. Tang,[2] and C. S. Chu[1]
[1]*Department of Electrophysics, National Chiao Tung University, Hsinchu 30010, Taiwan*
[2]*Physics Division, National Center for Theoretical Sciences, P.O. Box 2-131, Hsinchu 30013, Taiwan*
(Dated: December 9, 2004)

We propose and demonstrate theoretically that resonant inelastic scattering (RIS) can play an important role in dc spin current generation. The RIS makes it possible to generate dc spin current via a simple gate configuration: a single finger-gate that locates atop and orients transversely to a quantum channel in the presence of Rashba spin-orbit interaction. The ac biased finger-gate gives rise to a time-variation in the Rashba coupling parameter, which causes spin-resolved RIS, and subsequently contributes to the dc spin current. The spin current depends on both the static and the dynamic parts in the Rashba coupling parameter, α_0 and α_1, respectively, and is proportional to $\alpha_0\alpha_1^2$. The proposed gate configuration has the added advantage that no dc charge current is generated. Our study also shows that the spin current generation can be enhanced significantly in a double finger-gate configuration.

PACS numbers: 73.23.-b, 72.25.Dc, 72.30.+q, 72.25.-b

Spintronics is important in both application and fundamental arenas [1, 2]. A recent key issue of great interest is the generation of dc spin current (SC) without charge current. Various dc SC generation schemes have been proposed, involving static magnetic field [3, 4], ferromagnetic material [5], or ac magnetic field [6]. More recently, Rashba-type spin-orbit interaction in 2DEG [7, 8] has inspired attractive proposals for nonmagnetic dc SC generation [9–11]. Of these recent proposals, including a time-modulated quantum dot with a static spin-orbit coupling [9], and time-modulations of a barrier and the spin-orbit coupling parameter in two spatially separated regions [10], the working principle is basically adiabatic quantum pumping. Hence simultaneous generation of both dc spin and charge current is the norm. The condition of zero dc charge current, however, is met only for some judicious choices for the values of the system parameters.

It is known, on the other hand, that quantum transport in narrow channel exhibits RIS features when it is acted upon by a spatially localized time-modulated potential [12, 13]. This RIS is coherent inelastic scattering, but with resonance at work, when the traversing electrons can make transitions to their subband threshold by emitting $m\hbar\Omega$ [12, 13]. Should this RIS become spin-resolved in a Rashba-type quantum channel (RQC), of which its Rashba coupling parameter is time-modulated locally, we will have a simpler route to the nonmagnetic generation of dc SC. Thus we opt to study, in this Letter, the RIS features in a RQC. As is required by a study on the RIS features, our study goes beyond the adiabatic regime.

The system configuration considered is based on a RQC that forms out of a 2DEG in an asymmetric quantum well by the split-gate technique. As is depicted in Fig. 1(a), a finger gate (FG) is positioned above while it is separated from the RQC by an insulating layer. A local time-variation in the Rashba coupling parameter $\alpha(\mathbf{r},t)$ can be induced by ac biasing the FG [10, 11]. The Hamiltonian is given by $\mathcal{H} = p^2/2m + \mathcal{H}_{so}(\mathbf{r},t) + V_c(y)$ where the Rashba term

$$\mathcal{H}_{so}(\mathbf{r},t) = \mathbf{M}\cdot\frac{1}{2}\left[\alpha(\mathbf{r},t)\,p + p\,\alpha(\mathbf{r},t)\right]. \qquad (1)$$

Here $\mathbf{M} = \hat{z}\times\boldsymbol{\sigma}$, $\hat{z}$ is normal to the 2DEG, $\boldsymbol{\sigma}$ is the vector of Pauli spin matrices, and $V_c(y)$ is the confinement potential. The unperturbed Rashba coupling parameter $\alpha(\mathbf{r},t)$ is α_0 throughout the RQC, but when perturbed by the ac biased FG, it becomes $\alpha_0+\alpha_1\cos\Omega t$ in the region underneath the FG. The Dresselhaus term is neglected for the case of a narrow gap semiconductor system [14].

For a clear demonstration of the pumping mechanism, the unperturbed RQC we considered is narrow so that its subband energy spacing is much greater than the subband mixing due to the Rashba interaction. As such, the unperturbed Hamiltonian, in its dimensionless form, is $\mathcal{H}_0 = -\nabla^2 + \alpha_0\sigma_y(i\partial/\partial x) + V_c(y)$. Appropriate units have been used such that all physical quantities presented here, and henceforth, are dimensionless [13]. In particular, α is in unit of $v_F/2$, v_F indicating the Fermi velocity, and spin in unit of $\hbar/2$. The right-going (R) eigenstate of $\mathcal{H}_0$, in the n-th subband, is $\phi_n(y)\,\psi_n^\sigma(x)$, where $\psi_n^\sigma(x) = \exp\left[ik_{n,R}^\sigma x\right]\chi_\sigma$. The wavevector $k_{n,R}^\sigma = \sqrt{\mu_n} + \eta_\sigma\alpha_0/2$

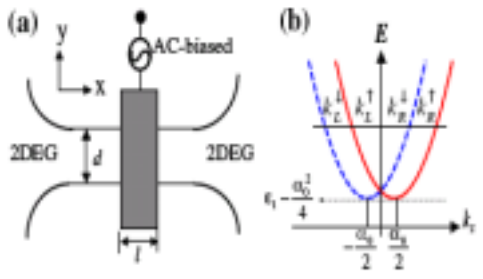

FIG. 1: (a) Top-view schematic illustration of the RQC. The ac-biased FG, of width l, is indicated by the grey area; (b) the electron dispersion relation of an unperturbed RQC.

while $\eta_\sigma = \pm 1$ denotes the eigenvalue of χ_σ to the operator σ_y. μ_n is the energy measured from the n-th subband threshold such that the energy of the eigentstate is $E = \mu_n + \varepsilon_n - \alpha_0^2/4$, for $\varepsilon_n = (n\pi/d)^2$. This dispersion relation is shown in Fig. 1(b). It is of import to note, for later reference, that right-going electrons have $|k_\uparrow^R| > |k_\downarrow^R|$, and that at the subband threshold $k_{\uparrow(\downarrow)}^R = k_{\uparrow(\downarrow)}^L$.

In the ac-biased region, $\mathcal{H} = \mathcal{H}_x + \mathcal{H}_y$, the transverse part $\mathcal{H}_y = -\partial^2/\partial y^2 + V_c(y)$, and the longitudinal part

$$\mathcal{H}_x(t) = \left(-i\frac{\partial}{\partial x} + \frac{\alpha(x,t)}{2}\mathbf{M}\cdot\hat{\boldsymbol{x}}\right)^2 - \frac{1}{4}\alpha(x,t)^2. \quad (2)$$

The form of Eq. (2) suggests an effective vector potential, $\mathbf{A}(t) = \frac{1}{2}\alpha(x,t)\mathbf{M}\cdot\hat{\boldsymbol{x}}$, which depends on the spin and gives rise to a spin-resolved driving electric field $\mathbf{E} = -\partial\mathbf{A}/\partial t$. However, in $\mathcal{H}_x$, the A^2 term does not depend on $\boldsymbol{\sigma}$, while for the term linear in $\mathbf{A}$, $\mathbf{A}\,\chi_\sigma = -\frac{1}{2}\eta_\sigma\,\alpha(x,t)\,\chi_\sigma$ gives rise only to a trivial spin dependence, which can be easily removed by a shift in the origin of time for the case of an oscillatory $\alpha(x,t)$. Yet it turns out that the full term linear in $\mathbf{A}$, given by $-i\frac{\partial}{\partial x}\hat{x}\cdot\mathbf{A}$, manages to give rise to nontrivial spin-resolved transmissions. In a perturbative sense, this term becomes $k_{\uparrow(\downarrow)}^R A_x$, for the case of a right-going electron incident upon a spatially uniform $\alpha(t)$. This renders the effective longitudinal driving field to become spin dependent. As a consequence, the difference in the current transmissions, for spin up and spin down cases, is proportional to α_0, and the difference is found to be amplified by RIS. In a RQC that has zero source-drain bias, the spin-resolved current transmission leads readily to dc spin current, but it cannot lead to dc charge current if the RQC is symmetric with respect to its source and drain.

An alternate way to understand the origin of the spin-resolved current transmission is presented in the following. Performing a unitary transformation $\Psi_\sigma(x,t) = \exp\left[(i\eta_\sigma/2)\int_{-l/2}^{x}\alpha(x',t)\,dx'\right]\psi_\sigma(x,t)$, the Schrödinger equation, Eq. (2), becomes

$$\left[-\frac{\partial^2}{\partial x^2} + U_1(t) + U_2^\sigma(t)\right]\psi_\sigma(x,t) = i\frac{\partial}{\partial t}\psi_\sigma(x,t), \quad (3)$$

of which the two time-dependent potentials are $U_1(t) = -\alpha(x,t)^2/4$, and $U_2^\sigma(t) = (\Omega\,\alpha_1/2)(x+l/2)\cos(\Omega t + \eta_\sigma\pi/2)$. Even though only U_2^σ depends on spin, both the term in $U_1(t)$ that oscillates with frequency Ω and U_2^σ together constitute a pair of quantum pumping potential that pump SC. This is our major finding in this work: that spin pumping nature is build-in even in a single FG configuration. Its origin is rooted in the intricate Rashab spin dynamics.

The expression for the pumped SC, in the absence of the source-drain bias, is obtained from the SC density operator

$$\hat{J}_x^y = i\left[\frac{\partial\Psi_\sigma^\dagger}{\partial x}\sigma_y\Psi_\sigma - \text{H. c.}\right] + \frac{\alpha}{2}\Psi_\sigma^\dagger\left\{\sigma_y, \mathbf{M}\right\}_x\Psi_\sigma. \quad (4)$$

The SC conservation is maintained due to the supression of subband mixing in a RQC, and the associated spin-flip mechanism. By taking the time-average of the transmitted and the incident SC in Eq. (4), and their ratio, we obtain the spin-resolved current transmission $T_{\beta\alpha}^\sigma$, where α, β, are, respectively, the incident and the transmitting lead. Summing over all possible incident states from both reservoirs R and L, the net SC is given by

$$\begin{aligned} I^s &= I^\uparrow + I^\downarrow \\ &= \int dE\, f(E)\left[\left(T_{RL}^\uparrow - T_{LR}^\uparrow\right) + \left(T_{LR}^\downarrow - T_{RL}^\downarrow\right)\right] \end{aligned} \quad (5)$$

where $f(E)$ is the Fermi-Dirac distribution, and $T_{RL}^\sigma = \sum_n\sum_{m(\mu_n^m>0)} T_{n,RL}^{m,\sigma}$. The transmission coefficient $T_{n,RL}^{m,\sigma} = \left|t_{n,RL}^{m,\sigma}\right|^2\sqrt{\mu_n^m/\mu_n}$ denotes the current transmission that an electron incident from terminal L in the spin channel σ, subband n, energy E, is scattered into terminal R, sideband m, with kinetic energy $\mu_n^m = \mu_n + m\Omega$. The net charge current is simply given by $I^q = I^\uparrow - I^\downarrow$. In a symmetric time-dependent FG configuration, we have $T_{LR}^\sigma = T_{RL}^{-\sigma}$, so that the net spin current is $I^s = 2\int dE\, f(E)\left(T_{RL}^\uparrow - T_{RL}^\downarrow\right)$ and the net charge current is identically zero.

Before we demonstrate numerically the robustness of the SC pumping, it is worthwhile to first look at the weak-pumping regime, which affords us analytical results. To this end, the scattering amplitudes are restricted to include only up to the sidebands $m = \pm 1$, that is, up to first power in α_1. For an electron incident with wave vector $k_{n,R}^\sigma$ from terminal L, the spin-resolved reflection amplitude is obtained to be

$$r_{n,LL}^{m,\sigma} = -m\eta_\sigma\left(\frac{\alpha_1}{2}\right)\frac{\left[e^{i\left(k_{n,R}^\sigma - k_{n,L}^{m,\sigma}\right)l} - 1\right]\left[\frac{1}{\Omega}k_{n,R}^\sigma\left(k_{n,R}^\sigma - k_{n,R}^{m,\sigma}\right) + \frac{m}{2}\right]}{k_{n,R}^{m,\sigma} - k_{n,L}^{m,\sigma}} \quad (6)$$

for $m = \pm 1$. The reflection amplitude $r^{0,\sigma}_{n,LL}$ is of order α_1^2, and is negligible in our weak-pumping approximation. Here the wave vector $k^{m,\sigma}_{n,R(L)} = \pm(\mu^m_n)^{1/2} + \eta_\sigma \alpha_0/2$, with upper (lower) sign corresponds to the right- (left-) moving electron in the nth subband, mth sideband, and with kinetic energy μ^m_n. It is obvious then that differences between wave vectors of different sideband indices, but of the same spin state, are spin independent. Hence the spin dependence of $r^{\pm 1,\sigma}_{n,LL}$ arises solely from the $k^\sigma_{n,R}$ in the numerator that does not involve in a wave vector difference. Furthermore, this spin dependence is associated with α_0. It is not unexpected then that the SC is proportional to α_0. The SC is related to the current transmission which, within the aforementioned approximation, is given by $T^\sigma_{RL} \approx 1 - \sum_n \left[R^{1,\sigma}_{n,LL} + R^{-1,\sigma}_{n,LL}\right]$, where $R^{m,\sigma}_{n,LL} = \left|r^{m,\sigma}_{n,LL}\right|^2 \sqrt{\mu^m_n}/\sqrt{\mu_n}$. From Eq. (5), the energy derivative of the zero temperature SC is given by $\partial I^s/\partial E = 2\Delta T_{RL} = 2(T^\uparrow_{RL} - T^\downarrow_{RL})$ from which its explicit expression is given by

$$\frac{\partial I^s}{\partial E} = \frac{1}{2}\alpha_0\alpha_1^2 \sum_n \sum_{\substack{m=\pm 1 \\ (\mu^m_n>0)}} \frac{\left[1-\cos\left(\left(\sqrt{\mu_n}+\sqrt{\mu^m_n}\right)l\right)\right]\left[\left(\frac{1}{4}\right)^2 - \left(\frac{1}{\Omega}\left(\mu_n - \sqrt{\mu_n\mu^m_n}\right) + \frac{m}{4}\right)^2\right]}{\mu_n\sqrt{\mu^m_n}}. \tag{7}$$

That this expression diverges when $\mu^m_n = 0$, for $m < 0$, exhibits the RIS feature unambiguously.

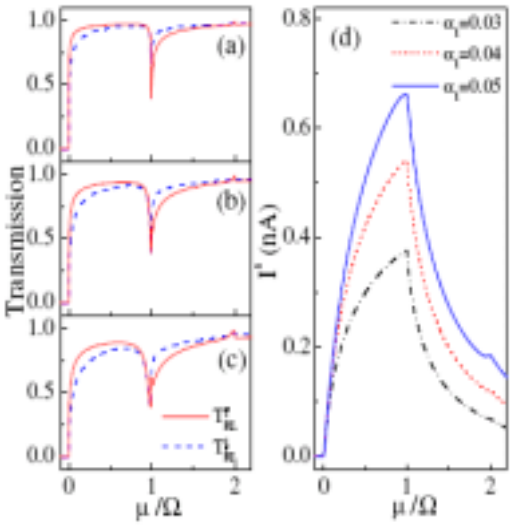

FIG. 2: Spin-resolved current transmissions $T^\uparrow_{RL}$ (solid) and $T^\downarrow_{RL}$ (dashed) versus the incident energy μ/Ω. Parameters $N = 1$, $\alpha_0 = 0.13$, $\Omega = 0.002$, $l = 20$, and with α_1 = (a) 0.03, (b) 0.04, and (c) 0.05. The corresponding dc SC is plotted in (d).

In the following, we present results obtained from solving the time-dependent spin-orbit scattering exactly, in the numerical sense [15]. Physical parameters are chosen to be consistent with the InGaAs-InAlAs based narrow gap heterostructures such that the electron density $n_e = 1 \times 10^{12}$ cm^{-2}, effective mass $m^* = 0.04 m_0$, and $\alpha_0 = 0.13$ ($\hbar\alpha_0 = 3 \times 10^{-11}$ eV m) [8]. Accordingly, the length unit $l^* = 4.0$ nm, and the energy unit $E^* = 59$ meV.

For the case of one FG ($N = 1$), the energy dependence of the spin-resolved transmission T^σ_{RL} is plotted in Figs. 2 (a)-(c), and that of the corresponding dc SC is plotted in Fig. 2 (d). The FG width $l = 20$ (80 nm), driving frequency $\Omega = 0.002$ ($\nu = \Omega/2\pi \approx 28$ GHz), and energy $\mu = E - \varepsilon_1$. Dip features in T^σ_{RL} at $\mu/\Omega = 1$ are the QBS features, where electrons undergo coherent inelastic scattering to a QBS just beneath its subband bottom [12]. Higer order QBS features at $\mu/\Omega = 2$ are barely shown by the small peaks. Of particular interest is the change in sign in the transmission difference $\Delta T_{RL} = T^\uparrow_{RL} - T^\downarrow_{RL}$ across the dip structures, namely, $\Delta T_{RL}(\mu = \Omega^-) > 0$ while $\Delta T_{RL}(\mu = \Omega^+) < 0$. This leads to a nonzero dc SC, and that it peaks at $\mu/\Omega = 1$, as is exhibited in Fig. 2(d). It is also shown that the dc SC increases with the oscillating amplitude α_1 of the ac-biased gate voltage.

The possibility of nonlinear enhancement in the dc SC by two FGs ($N = 2$) is presented in Figs. 3 (a)-(c). The driving frequency is chosen to be $\Omega = 0.001$ ($\nu \approx 14$ GHz), and the FG width $l = 22$ ($\simeq 88$ nm). For comparison, the $N = 1$ FG transmissions are plotted along side with that of the $N = 2$ FG case, in Figs. 3 (a), and (b), respectively. The corresponding dc SC, expressed in terms of pumped spin per cycle $N^s_P = (2\pi/\Omega)|I^s|$, is shown in Fig. 3(c). The pumping is optimized by a choice of the FG separation, with the edge to edge separation $\Delta l = 22$. That nonlinear effects are significant is supported by the appearance of up to the fourth-sideband QBS dip structures in Fig. 3(b). As indicated by arrows, the pumped spin per cycle peaks at $\mu/\Omega \simeq 1.57$ (1.92), and with peak value 0.8 (0.1) for the case of $N = 2$ ($N = 1$) FG. The enhancement in N^s_P is nonlinear, far greater than doubling the N^s_P of $N = 1$ FG.

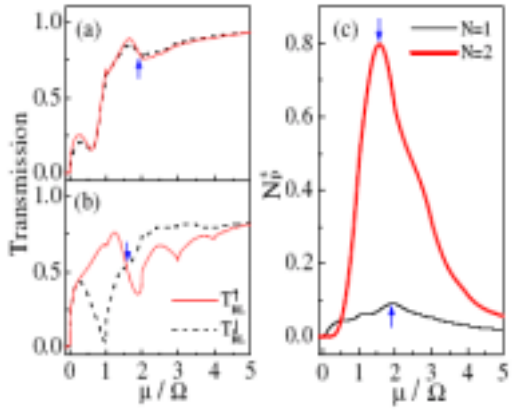

FIG. 3: Current transmission versus μ/Ω for N = (a) 1, and (b) 2. Pumped spins per cycle are plotted in (c) for $N = 1$ (thick curve) and $N = 2$ (thin curve) with driving frequency $\Omega = 0.001$ and $\alpha_1 = 0.065$. Other parameters are the same as in Fig. 2.

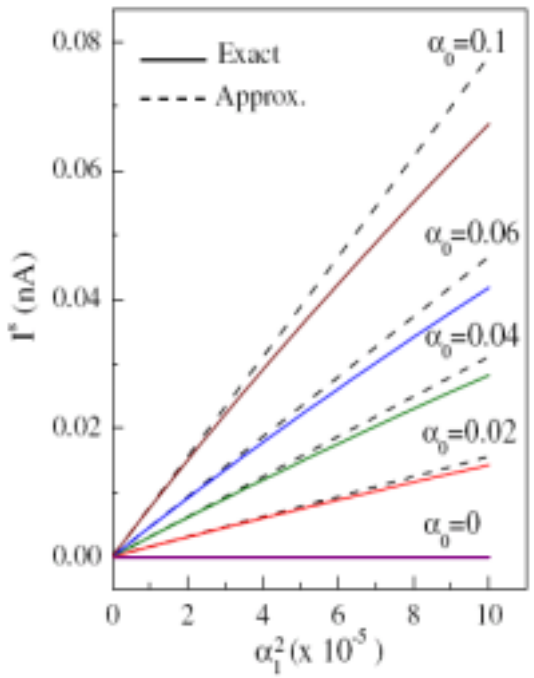

FIG. 4: Pumped dc SC versus α_1^2 for various α_0 values. Other parameters are $\Omega = 0.01$, $l = 20$, and $\mu = \Omega^+$.

In Fig. 4, we present the dependence of the dc SC peak values on the pumping parameters α_0 and α_1, and for the case of one FG. The numerical results, depicted by solid curves, coincide nicely, in the small α_1 regime, with the one sideband approximation results, depicted by broken curves, and calculated according to Eq. (7). This confirms that the dc SC is proportional to $\alpha_0\alpha_1^2$ in the weak pumping regime. Moreover, deviation of the numerical results from the weak pumping behavior sets in at smaller α_1 values when α_0 increases. Typical degree of deviation can be inferred from the case of $\alpha_0 = 0.1$ and $\alpha_1 = 0.01$, where the deviation of dc SC $\Delta I^s = |I^s_{\rm numerical} - I^s_{\rm app}|/I^s_{\rm numerical} \simeq 0.16$. We also find that, as Ω decreases, the degree of deviation increases, indicating the need to include more sidebands for the description of the time-dependent quantum scattering.

In conclusion, a nonmagnetic way of generating dc SC has been established. The proposed configuration, a Rashba-type quantum channel driven by an ac biasing finger gate, is relatively simple and is within reach of recent fabrication capability. The nature of the spin pumping is studied in detail and its pumping mechanism understood. Resonant inelastic process is found to be a major factor that contributes to the robustness of the spin pumping. The coherent nature of the pumping supports further enhancement of the spin pumping by invoking configuration consisting of more than one finger gates.

The authors acknowledge valuable discussions with A. G. Mal'shukov. This work was funded by the National Science Council of ROC under Grant Nos. NSC92-2112-M-009-035, NSC92-2120-M-009-010, NSC93-2112-M-009-036 and NSC93-2119-M-007-002 (NCTS).

[1] *Semiconductor Spintronics and Quantum Computation*, edited by D.D. Awschalom, N. Samarth, and D. Loss (Springer-Verlag, Berlin, 2002).
[2] S.A. Wolf *et al.*, Science **294**, 1488 (2001); Y. Kato *et al.*, *ibid.* **299**, 1201 (2003); S. Murakami *et al.*, *ibid.* **301**, 1348 (2003).
[3] E. R. Mucciolo, C. Chamon, and C. M. Marcus, Phys. Rev. Lett. **89**, 146802 (2002). Experimental realization was reported by S. K. Watson, R. M. Potok, C. M. Marcus, and V. Umansky in Phys. Rev. Lett. **91**, 258301 (2003).
[4] Q. F. Sun, H. Guo, and J. Wang, Phys. Rev. Lett. **90**, 258301 (2003).
[5] A. Brataas, Y. Tserkovnyak, G. E. W. Bauer, and B. I. Halperin, Phys. Rev. B **66** 60404 (2002).
[6] P. Zhang, Q. K. Xue, and X. C. Xie, Phys. Rev. Lett. **91**, 196602 (2003).
[7] Y. A. Bychkov and E. I. Rashba, J. Phys. C **17**, 6039 (1984).
[8] J. Nitta *et al.*, Phys. Rev. Lett. **78**, 1335 (1997); D. Grundler, *ibid.* **84**, 6074 (2000).
[9] P. Sharma and P. W. Brouwer, Phys. Rev. Lett. **91**, 166801 (2003).
[10] M. Governale, F. Taddei, and R. Fazio, Phys. Rev. B **68**, 155324 (2003).
[11] A. G. Mal'shukov, C. S. Tang, C. S. Chu, and K. A. Chao, Phys. Rev. B **68**, 23 3307 (2003).
[12] P. F. Bagwell and R. K. Lake, Phys. Rev. B **46**, 15329 (1992).
[13] C. S. Tang and C. S. Chu, Phys. Rev. B **53**, 4838 (1996).
[14] G. Lommer, F. Malcher, and U. Rössler, Phys. Rev. Lett. **60**, 728 (1988).
[15] L. Y. Wang, C. S. Tang, and C. S. Chu (unpublished).

[Reference]:

[1] C.M. Marcus, A.J. Rimberg, R.M. Wetervelt, P.F. Hopkins, and A.C. Gossard, Phys. Rev. Lett. **69**, 506 (1992).

[2] A.M. Chang, H.U. Baranger, L.N. Pfeiffer, and K.W. West, Phys. Rev. Lett. **73**, 2111 (1994).

[3] H.I. Chan, R.M. Clarke, C.M. Marcus, K. Campman, and A.C. Gossard, Phys. Rev. Lett. **74**, 3876 (1995).

[4] M. Persson, J. Pettersson, B. von Sydow, P.E. Lindelof, A. Kristensen, and K.-F. Berggren, Phys. Rev. B **52**, 8921 (1995).

[5] M.W. Keller, A. Mittal, J.W. Sleight, R.G. Wheeler, D.E. Prober, R.N. Sacks, and H. Shrtikmann, Phys. Rev. B **53**, R1693 (1996).

[6] Y. Wang, N. Zhu, and J. Wang, Phys. Rev. B **53**, 16 408 (1996).

[7] R. Akis, D.K. Ferry, and J.P. Bird, Phys. Rev. Lett. **79**, 123 (1997).

[8] I.V. Zozoulenko and T. Lundberg, Phys. Rev. Lett. **81**, 1744 (1998).

[9] R. Akis, D.K. Ferry, and J.P. Bird, Phys. Rev. Lett. **81**, 1745 (1998).

[10] J.P. Bird, R. Akis, D.K. Ferry, D. Vasileska, J. Cooper, Y. Aoyagi, and T. Sugano, Phys. Rev. Lett. **82**, 4691 (1999).

[11] A.P.S. de Moura, Y.-C. Lai, R. Akis, J.P. Bird, and D.K. Ferry, Phys. Rev. Lett. **88**, 236804 (2002).

[12] S. Datta and B. Das, Appl. Phys. Lett. **56**, 665 (1990).

[13] Yu.A. Bychkov and E.I. Rashba, J. Phys. C **17**, 6039 (1984).

[14] J. Nitta *et al.*, Phys. Rev. Lett. **78**, 1335 (1997); G. Engels *et al.* Phys. Rev. B **55**, R1958 (1997).

[15] D. Grundler, Phys. Rev. Lett. **84**, 6074 (2000).

[16] A.G. Mal'shukov, V. Shlyapin, and K.A. Chao, Phys. Rev. B **66**, 081311(R) (2002); J.C. Egues, G. Burkard, and D. Loss, cond-mat/0209682 (unpublished); M. Governale *et al.*, Phys. Rev. B **65**, 140403(R) (2002).

[17] D. J. Thouless, Phys. Rev. B **27**, 6083 (1983).

[18] Q. Niu, Phys. Rev. Lett. **64**, 1812 (1990).

[19] F. Hekking and Yu. V. Nazarov, Phys. Rev. B **44**, 9110 (1991).

[20] M. Switkes, C. M. Marcus, K. Campman, and A. C. Gossard, Science **283**, 1905 (1999).

[21] P. W. Brouwer, Phys. Rev. B **58**, R10135 (1998).

[22] I. L. Aleiner and A. V. Andreev, Phys. Rev. Lett. **81**, 1286 (1998).

[23] F. Zhou, B. Spivak, and B. Altshuler, Phys. Rev. Lett. **82**, 608 (1999).

[24] O. Entin-Wohlman and A. Aharony, Phys. Rev. B **66**, 035329 (2002).

[25] Y. Wei, J. Wang, and H. Guo, Phys. Rev. B **62**, 9947 (2000).

[26] C. S. Tang and C. S. Chu, Solid State Commun. **120**, 353 (2001).

[27] S. Zhu and Z. D. Wang, Phys. Rev. B **65**, 155313 (2002).

[28] M. L. Polianski and P. W. Brouwer, Phys. Rev. B **64**, 075304 (2001).

[29] J. E. Avron, A. Elgart, G. M. Graf, and L. Sadun, Phys. Rev. Lett. **87**, 236601 (2001).

[30] B. Wang and J. Wang, Phys. Rev. B **66**, 125310 (2002).

[31] M. Moskalets and M. Büttiker, Phys. Rev. B **64**, 201305(R) (2001).

[32] M. Moskalets and M. Büttiker, Phys. Rev. B **66**, 035306 (2002).

[33] S. W. Kim, Phys. Rev. B **68**, 085312 (2003); S. W. Kim, Phys. Rev. B **66**, 235304 (2002).

[34] M. Moskalets and M. Büttiker, Phys. Rev. B **68**, 075303 (2003).
[35] M. Moskalets and M. Büttiker, Phys. Rev. B **68**, 161311 (2003).
[36] D. Cohen, Phys. Rev. B **68**, 201303(R) (2003).
[37] P. Sharma and C. Chamon, Phys. Rev. B **68**, 035321 (2003).
[38] *Semiconductor Spintronics and Quantum Computation*, edited by D.D. Awschalom, N. Samarth, and D. Loss (Springer-Verlag, Berlin, 2002).
[39] S.A. Wolf *et al.*, Science 294, 1488 (2001); Y. Kato *et al.*, *ibid.* 299, 1201 (2003); S. Murakami *et al.*, *ibid.* 301, 1348 (2003).
[40] E. R. Mucciolo, C. Chamon, and C. M. Marcus, Phys. Rev. Lett. 89, 146802 (2002). Experimental realization was reported by S. K. Watson, R. M. Potok, C. M. Marcus, and V. Umansky in Phys. Rev. Lett. 91, 258301 (2003).
[41] Q. F. Sun, H. Guo, and J. Wang, Phys. Rev. Lett. 90, 258301 (2003).
[42] A. Brataas, Y. Tserkovnyak, G. E. W. Bauer, and B. I. Halperin, Phys. Rev. B 66 60404 (2002).
[43] P. Zhang, Q. K. Xue, and X. C. Xie, Phys. Rev. Lett. 91, 196602 (2003).
[44] Y. A. Bychkov and E. I. Rashba, J. Phys. C 17, 6039 (1984).
[45] J. Nitta *et al.*, Phys. Rev. Lett. 78, 1335 (1997); D. Grundler, *ibid.* 84, 6074 (2000).
[46] P. Sharma and P. W. Brouwer, Phys. Rev. Lett. 91, 166801 (2003).
[47] M. Governale, F. Taddei, and R. Fazio, Phys. Rev. B 68, 155324 (2003).
[48] A. G. Mal'shukov, C. S. Tang, C. S. Chu, and K. A. Chao, Phys. Rev. B **68**, 23 3307 (2003).
[49] Y. Imry, *Introduction to Mesoscopic Physics* (Oxford University Press, New York, 1997).
[50] M. *B*Ä*uttiker* and R. Landauer, Phys. Rev. Lett. **49**, 1739(1982).
[51] U. Fano, Phys Rev. **124**, 1866 (1961).
[52] U. Fano and A. R. P. Rau, Atomic Collision and Spectra (Academic Press, Orlando, 1986).
[53] J. Faist, F. Capasso, C. Sirtori, K. W. West, and L. N. Pfei_er, Nature **390**, 589 (1997).
[54] F. Cerdeira, T. A, Fjeldly, and M. Cardona, Phys. Rev. B **8**, 4743 (1973).
[55] R. K. Adair, C. K. Bockelman, and R. E. Peterson, Phys. Rev. **76**, 308 (1949).
[56] V. Madhavan, W. Chen, T. Jamneala, M. F. Crommie, and N. S. Wingreen, Science **280**, 567 (1998).
[57] J. Li, W.-D. Schneider, R. Berndt, and B. Delly, Phys. Rev. Lett. **80**, 2893 (1998).
[58] C. Fuhner, U. F. Keyser, R. J. Haug, D. Reuter, and A. D. Wieck, cond-mat/0307590.
[59] J. Gores, D. Goldhaber-Gordon, S. Heemeyer, M. A. Kastner, H. Shtrikman, D. Mahalu, and Y. Meirev, Phys. Rev. B **62**, 2188 (2000).
[60] I. G. Zacharia, D. Goldhaber-Gordon, G. Granger, M. A. Kastner, Y. B. Khavin, H. Shtrikman, D. Mahalu, and U. Meirav, Phys. Rev. B. **64**, 155311 (2001).
[61] K. Kobayashi, H. Aikawa, S. Katsumoto, and Y. Iye, Phys. Rev. Lett. **88**, 256806 (2002).
[62] K. Kobayashi, H. Aikawa, A. Sano, S. Katsumoto, and Y. Iye, Phys. Rev. B **70**, 35319 (2004).
[63] M. Sato, H. Aikawa, K. Kobayashi, S. Katsumoto, and Y. Iye, cond-mat/0410062.
[64] J. Kim, J.-R. Kim, J.-O Lee, J. W. Park, H. M. So, N. Kim, K. Kang, K.-H. Yoo, and J.-J. Kim, Phys. Rev. Lett **90**, 166403 (2003).
[65] A. A. Clerk, X. Waintal, and P. W. Brouwer, Phys. Rev. Lett. **86**, 4636 (2001).
[66] Y.-J. Xiong and S.-J. Xiong, Int. J. Mod. Phys. B **16**, 1479 (2002).

[67] J. F. Song, Y. Ochiai, and J. P. Bird, Appl. Phys. Lett. **82**, 4561 (2003).
[68] C. S. Tang, Y. H. Tan, and C. S. Chu, Phys. Rev. B **67**, 2053241 (2003).
[69] A. G. Mal'shukov, C. S. Tang, C. S. Chu, and K. A. Chao, Phys. Rev. B **68**, 2333071 (2003).
[70] S. W. Chung, C. S. Tang, Y. H. Tan, C. S. Chu, and C. Y. Chang, Phys. Rev. B **67**, 0853151 (2004).
[71] L. Y. Wang, C. S. Tang, and C. S. Chu, cond-mat/0409291.

[72] *Conference papers:*

The 2004 annual meeting of the Physical Society of the Republic of China

[C1] S. W. Chung, C. S. Tang, and C. S. Chu, "Quantum charge pumping induced by finger-gate array."
Oral section: TF-8 (2004/02/10).

[C2] L. Y. Wang, C. S. Tang, and C. S. Chu, "Generation of spin currents by AC biased finger gates in a quantum channel."
Oral section: TM-5 (2004/02/10).

[C3] Y. Y. Lin, C. S. Tang, and C. S. Chu, "Effect of random impurities on the conductance of a quantum wire."
Oral section: PP-18.
Post paper.

[73] *Papers in preparation:*

[P1] C. W. Wu, and C. S. Chu, "Effect of an oscillating potential on the persistent transition in a mesoscopic ring." (in preparation)

[P2] K. K. Voo, and C. S. Chu, "Fano resonance in transport through a mesoscopic two-lead ring." (in preparation)